SLAC-PUB-13622

May 2009

To be submitted to Astrophysical Journal - Not Yet Refereed

Bright AGN Source List from the First Three Months of the *Fermi* Large Area Telescope All-Sky Survey

A. A. Abdo[1,2], M. Ackermann[3], M. Ajello[3], W. B. Atwood[4], M. Axelsson[5,6], L. Baldini[7], J. Ballet[8], G. Barbiellini[9,10], D. Bastieri[11,12], B. M. Baughman[13], K. Bechtol[3], R. Bellazzini[7], R. D. Blandford[3], E. D. Bloom[3], E. Bonamente[14,15], A. W. Borgland[3], J. Bregeon[7], A. Brez[7], M. Brigida[16,17], P. Bruel[18], T. H. Burnett[19], G. A. Caliandro[16,17], R. A. Cameron[3], P. A. Caraveo[20], J. M. Casandjian[8], E. Cavazzuti[21], C. Cecchi[14,15], E. Charles[3], A. Chekhtman[22,2], A. W. Chen[20], C. C. Cheung[23], J. Chiang[3], S. Ciprini[14,15], R. Claus[3], J. Cohen-Tanugi[24], S. Colafrancesco[21], W. Collmar[25], J. Conrad[5,26,27], L. Costamante[3], S. Cutini[21], C. D. Dermer[2], A. de Angelis[28], F. de Palma[16,17], S. W. Digel[3], E. do Couto e Silva[3], P. S. Drell[3], R. Dubois[3], D. Dumora[29,30], C. Farnier[24], C. Favuzzi[16,17], S. J. Fegan[18], E. C. Ferrara[23], J. Finke[1,2], W. B. Focke[3], L. Foschini[31], M. Frailis[28], L. Fuhrmann[32], Y. Fukazawa[33], S. Funk[3], P. Fusco[16,17], F. Gargano[17], D. Gasparrini[21], N. Gehrels[23,34], S. Germani[14,15], B. Giebels[18], N. Giglietto[16,17], P. Giommi[21], F. Giordano[16,17], M. Giroletti[35], T. Glanzman[3], G. Godfrey[3], I. A. Grenier[8], M.-H. Grondin[29,30], J. E. Grove[2], L. Guillemot[29,30], S. Guiriec[24], Y. Hanabata[33], A. K. Harding[23], R. C. Hartman[23], M. Hayashida[3], E. Hays[23], S. E. Healey[3], D. Horan[18], G. Jóhannesson[3], R. P. Johnson[4], T. J. Johnson[23,34], W. N. Johnson[2], M. Kadler[36,37,38,39], T. Kamae[3], H. Katagiri[33], J. Kataoka[40], M. Kerr[19], J. Knödlseder[41], M. L. Kocian[3], F. Kuehn[13], M. Kuss[7], J. Lande[3], L. Latronico[7], M. Lemoine-Goumard[29,30], F. Longo[9,10], F. Loparco[16,17], B. Lott[29,30,⋆], M. N. Lovellette[2], P. Lubrano[14,15], G. M. Madejski[3], A. Makeev[22,2], M. N. Mazziotta[17], W. McConville[23], J. E. McEnery[23], C. Meurer[5,27], P. F. Michelson[3], W. Mitthumsiri[3], T. Mizuno[33], A. A. Moiseev[37], C. Monte[16,17], M. E. Monzani[3], A. Morselli[42], I. V. Moskalenko[3], S. Murgia[3], P. L. Nolan[3], J. P. Norris[43], E. Nuss[24], T. Ohsugi[33], N. Omodei[7], E. Orlando[25], J. F. Ormes[43], D. Paneque[3], J. H. Panetta[3], D. Parent[29,30], V. Pelassa[24], M. Pepe[14,15], M. Pesce-Rollins[7], F. Piron[24], T. A. Porter[4], S. Rainò[16,17], R. Rando[11,12], M. Razzano[7], S. Razzaque[1,2], A. Reimer[3], O. Reimer[3], T. Reposeur[29,30], L. C. Reyes[44], S. Ritz[23,34], A. Y. Rodriguez[45], R. W. Romani[3], F. Ryde[5,26], H. F.-W. Sadrozinski[4], D. Sanchez[18], A. Sander[13], P. M. Saz Parkinson[4], J. D. Scargle[46], T. L. Schalk[4], A. Sellerholm[5,27], C. Sgrò[7], M. Shaw[3], D. A. Smith[29,30], P. D. Smith[13], G. Spandre[7], P. Spinelli[16,17], J.-L. Starck[8], M. S. Strickman[2], D. J. Suson[47], H. Tajima[3], H. Takahashi[33], T. Takahashi[48], T. Tanaka[3], G. B. Taylor[49], J. B. Thayer[3], J. G. Thayer[3], D. J. Thompson[23], L. Tibaldo[11,12], D. F. Torres[50,45], G. Tosti[14,15,⋆], A. Tramacere[51,3], Y. Uchiyama[3], T. L. Usher[3], N. Vilchez[41], M. Villata[52], V. Vitale[42,53], A. P. Waite[3], B. L. Winer[13], K. S. Wood[2], T. Ylinen[54,5,26], M. Ziegler[4]

Work supported in part by US Department of Energy contract DE-AC02-76SF00515

[1] National Research Council Research Associate

[2] Space Science Division, Naval Research Laboratory, Washington, DC 20375

[3] W. W. Hansen Experimental Physics Laboratory, Kavli Institute for Particle Astrophysics and Cosmology, Department of Physics and Stanford Linear Accelerator Center, Stanford University, Stanford, CA 94305

[4] Santa Cruz Institute for Particle Physics, Department of Physics and Department of Astronomy and Astrophysics, University of California at Santa Cruz, Santa Cruz, CA 95064

[5] The Oskar Klein Centre for Cosmo Particle Physics, AlbaNova, SE-106 91 Stockholm, Sweden

[6] Stockholm Observatory, Albanova, SE-106 91 Stockholm, Sweden

[7] Istituto Nazionale di Fisica Nucleare, Sezione di Pisa, I-56127 Pisa, Italy

[8] Laboratoire AIM, CEA-IRFU/CNRS/Université Paris Diderot, Service d'Astrophysique, CEA Saclay, 91191 Gif sur Yvette, France

[9] Istituto Nazionale di Fisica Nucleare, Sezione di Trieste, I-34127 Trieste, Italy

[10] Dipartimento di Fisica, Università di Trieste, I-34127 Trieste, Italy

[11] Istituto Nazionale di Fisica Nucleare, Sezione di Padova, I-35131 Padova, Italy

[12] Dipartimento di Fisica "G. Galilei", Università di Padova, I-35131 Padova, Italy

[13] Department of Physics, Center for Cosmology and Astro-Particle Physics, The Ohio State University, Columbus, OH 43210

[14] Istituto Nazionale di Fisica Nucleare, Sezione di Perugia, I-06123 Perugia, Italy

[15] Dipartimento di Fisica, Università degli Studi di Perugia, I-06123 Perugia, Italy

[16] Dipartimento di Fisica "M. Merlin" dell'Università e del Politecnico di Bari, I-70126 Bari, Italy

[17] Istituto Nazionale di Fisica Nucleare, Sezione di Bari, 70126 Bari, Italy

[18] Laboratoire Leprince-Ringuet, École polytechnique, CNRS/IN2P3, Palaiseau, France

[19] Department of Physics, University of Washington, Seattle, WA 98195-1560

[20] INAF-Istituto di Astrofisica Spaziale e Fisica Cosmica, I-20133 Milano, Italy

[21] Agenzia Spaziale Italiana (ASI) Science Data Center, I-00044 Frascati (Roma), Italy

[22] George Mason University, Fairfax, VA 22030

[23] NASA Goddard Space Flight Center, Greenbelt, MD 20771

[24] Laboratoire de Physique Théorique et Astroparticules, Université Montpellier 2, CNRS/IN2P3, Montpellier, France

[25] Max-Planck Institut für extraterrestrische Physik, 85748 Garching, Germany

[26] Department of Physics, Royal Institute of Technology (KTH), AlbaNova, SE-106 91 Stockholm, Sweden

[27] Department of Physics, Stockholm University, AlbaNova, SE-106 91 Stockholm, Sweden

[28] Dipartimento di Fisica, Università di Udine and Istituto Nazionale di Fisica Nucleare, Sezione di Trieste, Gruppo Collegato di Udine, I-33100 Udine, Italy

[29] CNRS/IN2P3, Centre d'Études Nucléaires Bordeaux Gradignan, UMR 5797, Gradignan, 33175, France

ABSTRACT

The first three months of sky-survey operation with the *Fermi Gamma Ray Space Telescope (Fermi)* Large Area Telescope (LAT) reveals 132 bright sources at |b| >10° with test statistic greater than 100 (corresponding to about 10σ). Two methods, based on the CGRaBS, CRATES and BZCat catalogs, indicate high-confidence associations of 106 of these sources with known AGNs. This sample is referred to as the LAT Bright

[30] Université de Bordeaux, Centre d'Études Nucléaires Bordeaux Gradignan, UMR 5797, Gradignan, 33175, France

[31] INAF-IASF Bologna, 40129 Bologna, Italy

[32] Max-Planck-Institut für Radioastronomie, Auf dem Hügel 69, 53121 Bonn, Germany

[33] Department of Physical Science and Hiroshima Astrophysical Science Center, Hiroshima University, Higashi-Hiroshima 739-8526, Japan

[34] University of Maryland, College Park, MD 20742

[35] INAF Istituto di Radioastronomia, 40129 Bologna, Italy

[36] Dr. Remeis-Sternwarte Bamberg, Sternwartstrasse 7, D-96049 Bamberg, Germany

[37] Center for Research and Exploration in Space Science and Technology (CRESST), NASA Goddard Space Flight Center, Greenbelt, MD 20771

[38] Erlangen Centre for Astroparticle Physics, D-91058 Erlangen, Germany

[39] Universities Space Research Association (USRA), Columbia, MD 21044

[40] Department of Physics, Tokyo Institute of Technology, Meguro City, Tokyo 152-8551, Japan

[41] Centre d'Étude Spatiale des Rayonnements, CNRS/UPS, BP 44346, F-30128 Toulouse Cedex 4, France

[42] Istituto Nazionale di Fisica Nucleare, Sezione di Roma "Tor Vergata", I-00133 Roma, Italy

[43] Department of Physics and Astronomy, University of Denver, Denver, CO 80208

[44] Kavli Institute for Cosmological Physics, University of Chicago, Chicago, IL 60637

[45] Institut de Ciencies de l'Espai (IEEC-CSIC), Campus UAB, 08193 Barcelona, Spain

[46] Space Sciences Division, NASA Ames Research Center, Moffett Field, CA 94035-1000

[47] Department of Chemistry and Physics, Purdue University Calumet, Hammond, IN 46323-2094

[48] Institute of Space and Astronautical Science, JAXA, 3-1-1 Yoshinodai, Sagamihara, Kanagawa 229-8510, Japan

[49] University of New Mexico, MSC07 4220, Albuquerque, NM 87131

[50] Institució Catalana de Recerca i Estudis Avançats (ICREA), Barcelona, Spain

[51] Consorzio Interuniversitario per la Fisica Spaziale (CIFS), I-10133 Torino, Italy

[52] INAF, Osservatorio Astronomico di Torino, I-10025 Pino Torinese (TO), Italy

[53] Dipartimento di Fisica, Università di Roma "Tor Vergata", I-00133 Roma, Italy

[54] School of Pure and Applied Natural Sciences, University of Kalmar, SE-391 82 Kalmar, Sweden

[*] Corresponding authors: B. Lott, lott@cenbg.in2p3.fr; G. Tosti, tosti@pg.infn.it

AGN Sample (LBAS). It contains two radio galaxies, namely Centaurus A and NGC 1275, and 104 blazars consisting of 57 flat spectrum radio quasars (FSRQs), 42 BL Lac objects, and 5 blazars with uncertain classification. Four new blazars were discovered on the basis of the LAT detections. Remarkably, the LBAS includes 10 high-energy peaked BL Lacs (HBLs), sources which were so far hard to detect in the GeV range. Another 10 lower-confidence associations are found. Only thirty three of the sources, plus two at $|b| < 10°$, were previously detected with *EGRET*, probably due to the variable nature of these sources. The analysis of the gamma-ray properties of the LBAS sources reveals that the average GeV spectra of BL Lac objects are significantly harder than the spectra of FSRQs. No significant correlation between radio and peak gamma-ray fluxes is observed. Blazar log N - log S and luminosity functions are constructed to investigate the evolution of the different blazar classes, with positive evolution indicated for FSRQs but none for BLLacs. The contribution of LAT-blazars to the total extragalactic γ-ray intensity is estimated.

Subject headings: gamma rays: observations — galaxies: active — galaxies: jets — BL Lacertae objects: general

1. Introduction

The *Gamma ray Large Area Space Telescope* (*GLAST*) was launched on 11 June 2008, and renamed the *Fermi Gamma Ray Space Telescope* shortly after entering its scientific operating mission, which began on 11 August, 2008. The Large Area Telescope (LAT) on *Fermi* provides an increase in sensitivity by more than an order-of-magnitude over its predecessor *EGRET*, the Energetic Gamma Ray Experiment Telescope on the *Compton Gamma Ray Observatory* (Thompson et al. 1993), and the Italian Space Agency Satellite *AGILE* (Astro-rivelatore Gamma a Immagini Leggero; Tavani et al. 2008). In sky survey mode, the LAT observes all parts of the sky every 3 hours, providing effectively uniform exposure on longer timescales.

One of the major scientific goals of the *Fermi Gamma Ray Space Telescope* is to provide new data about γ-ray activity of AGNs. Rapidly varying fluxes and large luminosities of extragalactic γ-ray sources are best explained if the γ rays are emitted from collimated jets of charged particles moving at relativistic speeds (Blandford & Rees 1978; Maraschi et al. 1992). *Fermi*-LAT observations will help determine how these particles are accelerated, where the gamma rays are emitted, what the energy and power budgets of the supermassive black-hole engines are, what this says for the fueling and growth of black holes, and the reasons for the differences between radio-loud and radio-quiet AGNs, and FSRQs and BL Lac objects. These are just a few of the questions that γ-ray AGN studies with the *Fermi*-LAT are helping to answer (see Atwood et al. 2009, for more discussion of these goals).

In a companion publication (Abdo et al. 2009c), 132 bright sources at $|b| > 10°$ with test statistic (TS) > 100 are found in the preliminary three month *Fermi* all-sky survey. As expected from the EGRET legacy, a large fraction of these sources are AGNs. Detailed results of the subset of the *Fermi* bright source list that are associated with AGNs are presented here.

Sixty-six high-confidence blazars are listed in the Third *EGRET* catalog of high-energy gamma-ray sources (3EG catalog; Hartman et al. 1999), with the majority of them, ≈ 77%, identified as flat spectrum radio quasars (FSRQs), and the remaining ≈ 23% identified as belonging to the BL Lac class.[1] The recently released catalog of high-confidence *AGILE* gamma-ray sources[2] (Pittori et al. 2008) shows a somewhat higher percentage of BL Lacs. Unlike AGN surveys at optical or X-ray energies, in which the majority of AGNs are radio quiet (e.g., della Ceca et al. 1994; Ivezić et al. 2002), all AGNs detected at $\gtrsim 100$ MeV energies are also significant radio sources. This includes the 3EG and *AGILE* blazars, which are so far identified with flat spectrum (radio spectral index $\alpha_r > -0.5$ at GHz frequencies) radio-loud AGNs, and most show superluminal motion (Jorstad et al. 2001; Kellermann et al. 2004). Moreover, the redshift distribution is broad, with the largest redshift AGN known in the 3EG catalog at $z = 2.286$.

Here we present a source list of bright AGNs found in the set of the 132 bright LAT sources at $|b| > 10°$. Identification of variable γ-ray sources with blazars depends on the statistical likelihood of positional association and correlated variability of the γ-ray emissions with lower-frequency radiations (e.g. Sowards-Emmerd et al. 2003). The 106 sources having high-confidence associations with known blazars and radio-galaxies constitute the LAT Bright AGN Sample (LBAS). Included in this list are mean fluxes, weekly peak fluxes, spectral indices, locations, and variability information. Only sources with confidence levels greater than 10σ are retained in the LBAS. This list is not, however, complete, as we already know of many more sources at lower significance. The limiting flux depends on both the source sky location and the spectral hardness.

In Section 2, observations with the LAT, analysis methods, and the source detection procedure are presented. Section 3 describes the association method and gives the list of bright *Fermi*-LAT detected blazars. Key properties of the LBAS, including flux and spectral index, are presented in Section 4. The LBAS is compared with *EGRET* blazars in Section 5. Section 6 considers the radio/gamma-ray connection. Population studies, including source types and redshifts, are presented in Section 7, where the $\log N - \log S$ flux distributions and luminosity functions of the LBAS are constructed. The results are discussed in Section 8, including implications of the results for blazar evolution. We summarize in Section 9.

In the following we use a ΛCDM cosmology with values given within 1σ of the WMAP results (Komatsu et al. 2008), namely $h = 0.71$, $\Omega_m = 0.27$ and $\Omega_\Lambda = 0.73$. Here the Hubble constant

---

[1] In contrast to the prominent optical emission lines found in FSRQs, BL Lac objects are radio-loud, rapidly variable sources displaying nearly featureless continua with emission-line equivalent widths < 5 Å (for review, see Urry & Padovani 1995).

[2] http://www.asdc.asi.it/agilebrightcat/

$H_0 = 100h$ km s^{-1} Mpc^{-1} is used.

2. Observations with the Large Area Telescope

The *Fermi*-LAT is a pair-conversion gamma-ray telescope sensitive to photon energies greater than 20 MeV. It is made of a tracker (composed of two sections, front and back, with different capabilities), a calorimeter and an anticoincidence system to reject the charged-particle background. The LAT has a large peak effective area (~ 8000 cm^2 for 1 GeV photons in the event class considered here), viewing ≈ 2.4 sr of the full sky with excellent angular resolution (68% containment radius $\approx 1^\circ$ at $E = 1$ GeV for the front section of the tracker and about a factor of 2 larger for the back section). A full description of the LAT instrument and its predicted performance are reported in Atwood et al. (2009). During the first year, the telescope operates in sky-survey mode observing the whole sky every 3 hours. The overall coverage of the sky is fairly uniform, with variations of around $\simeq$15% around the mean value.

The LAT data used here were collected during the first 3-month all-sky survey, from August 4 to October 30 2008. We refer to the companion paper (Abdo et al. 2009c) for a full description of the data selection and analysis. In order to avoid background contamination from the bright Earth limb, time intervals where the Earth entered the LAT Field-of-View (FoV) were excluded from this study (corresponding to a rocking angle < 47 deg). In addition, events that were reconstructed within 8° of the Earth limb were excluded from the analysis (corresponding to a zenith angle cut of 105°). Due to uncertainties in the current calibration, only photons belonging to the "Diffuse" class with energies above 100 MeV were retained. These photons provide the purest gamma-ray dataset. The energy range was even more restricted in the source detection and spectral fitting analyses described below, where only photons with E >200 MeV were selected. The list of sources reported in Tables 1 and 2 was obtained as the result of the source detection, localization and significance estimate analyses described in detail in Abdo et al. (2009c).

The source detection step made use of two wavelet algorithms, (*mr_filter*) (Starck & Pierre 1998) and (*PGWAVE*) (Ciprini et al. 2007). The algorithms were run independently for different energy bands associated with different localization power and the results were cross-checked. The positions of the sources for which the detection significance was above threshold (4σ) were then refined using (*pointfit*), a simplified likelihood method (see Abdo et al. (2009c)). This algorithm uses photons with E>500 MeV and returns the optimized sky position as well as an estimate of the error radius for most detected sources. As discussed in Abdo et al. (2009c), the final error in the source position was estimated by multiplying the error radius returned by the algorithm by a factor close to 1.4 and adding 0.04° in quadrature (estimated from the residuals between the estimated and expected position of Vela). The 95% confidence error radius was then evaluated assuming a 2-D normal distribution.

To better estimate the source significance, we used the maximum likelihood algorithm implemented in (*gtlike*) a tool that is part of the standard *Fermi*-LAT *ScienceTools* software package[3]. The flux, photon index and test statistic (TS) of each source in the energy range 0.2-100 GeV were determined by analyzing regions of interest (ROI) typically 15° in radius. The model of the ROI used to fit the data was built taking into account of all the sources detected within a given ROI. The isotropic background and Galactic Diffuse background models used in the fit are discussed in Abdo et al. (2009c). Each source was modeled with a simple power law ($kE^{-\Gamma}$) for photons E> 200 MeV. The flux [E>100 MeV] (F_{100}), which is conventionally reported, was then calculated with the fitted parameters. This flux will be used throughout this paper. The spectral energy distributions of some bright sources show clear evidence for a break or curvature. A fit with a single power law function is certainly not the most appropriate choice for these sources but the resulting photon index does reflect the spectral hardness. A more detailed spectral analysis of the LBAS sources is beyond the scope of this paper. The source fluxes were also estimated by fitting independent power law functions in two energy bands (0.1-1 GeV) and (1-100 GeV) and summing up the two obtained fluxes. These fluxes ($F_2$5 in Table 3) are the same as those reported in the *Fermi* bright source list paper (Abdo et al. 2009c). For most sources, the fluxes obtained by the two methods are consistent within 30%.

The same procedure was applied to generate weekly light curves (spanning a 12-week period). From those, the weekly peak flux as well as a variability index (corresponding to a simple χ^2 criterion) were derived. The variability tag reported in this paper is set for sources associated with a probability of being constant lower than 1%. A few representative light curves are displayed in Fig. 1.

This analysis was performed with the preflight instrument response functions (P6_V1). In flight, the presence of pile-up signals in the LAT tracker and calorimeter left by earlier particles was revealed in periodic-trigger events. This feature leads to a reduction of the real acceptance as compared to the predicted one as fewer events pass the rejection cuts, most notably for low-energy photons. The magnitude of this reduction is still under investigation, but the fluxes reported here may be lower than the true ones by as much as 30% and the photon indices greater than the true ones by as much as 0.1 (true spectra could be softer by 0.1 unit in the photon index). Because of the current uncertainty, no correction has been applied to the results. This uncertainty applies uniformly to all sources. Our relative errors are much smaller (about 3% on the flux, Abdo et al. 2009c). With the acceptance used in this analysis, the measured fluxes of the 3 bright pulsars, Vela, Geminga and Crab (Abdo et al. 2009c) are found to be compatible within 11% with those reported in the 3EG catalog.

Fig. 2 shows the 3-month flux sensitivity for TS=100 and a photon index=2.2 as a function of the sky position, calculated by a semi-analytical, maximum likelihood estimate of the significance. This estimate takes the actual exposure, the PSF and the different backgrounds (galactic diffuse, extragalactic diffuse and instrumental) into account. The limiting flux is higher at low galactic

[3]http://fermi.gsfc.nasa.gov/ssc/data/analysis/documentation/Cicerone/

latitude due to a higher galactic diffuse background and close to the celestial south pole (l $\simeq 302°$, b $\simeq -27°$) where the exposure is lower.

The final result of the detection analysis is a list of 205 sources with a (TS > 100, $\sim 10\sigma$), composing the LAT Bright Source (0FGL) list (see Table 6. in Abdo et al. 2009c). For comparison, 31 sources detected by EGRET have a significance greater than 10σ in the 3EG (Hartman et al. 1999) and EGR (Casandjian & Grenier 2008) catalogs. Of these, only 13 were detected at $|b| > 10°$. In the 0FGL, a total of 132 sources, including 7 pulsars, are present at $|b| > 10°$. We have explored the possibility of associating AGNs with the 125 remaining sources.

3. Source association

Any source association procedure primarily relies on spatial coincidence. Fig. 3 shows the 95% error radius vs (TS) for the sources considered here. This radius depends on both the flux and the photon index, with a mean of 0.14°. For comparison, the average corresponding radius for the blazars in the 18 month *EGRET* sky survey is 0.62°. Of the 186 $|b| > 10°$ 3EG sources, 66 (35%) had "high" (but unspecified) confidence positional associations with blazars in the 3EG catalog. Another 27 positional coincidences were noted at lower significance. Although subsequent work (e.g. Mattox et al. 2001; Sowards-Emmerd et al. 2003) did find additional associations, ∼40% of the high-latitude 3EG sources remained unidentified.

Although the LAT localization accuracy is much better than those of previous gamma-ray telescopes, it is not good enough to enable a firm identification of a LAT source based solely on spatial coincidence. For the LAT, a firm identification is assumed only if correlated variability is observed at different wavelengths. In order to find associations between LAT sources and AGNs, two different approaches were pursued. The first method is based on a procedure similar to that developed by Sowards-Emmerd et al. (2003) for associating *EGRET* blazars with radio counterparts using an observational figure of merit (FoM). The second one is based on the calculation of source association probabilities following a Bayesian approach (de Ruiter et al. 1977; Sutherland & Saunders 1992), similar to that used by Mattox et al. (2001) to associate *EGRET* sources with radio sources. This method is described in Abdo et al. (2009c).

Several catalogs were used by the two association methods, the most important ones being the Combined Radio All-Sky Targeted Eight GHz Survey (CRATES; Healey et al. 2007) catalog and the *Roma-BZCAT*[4] (Massaro et al. 2007). The CRATES catalog contains precise positions, 8.4 GHz flux densities, and radio spectral indices for more than 11,000 flat-spectrum sources over the entire $|b| > 10°$ sky. The *Roma-BZCAT* is a master list of blazars based on an accurate examination of literature data and presently includes about 2700 sources, all observed at radio and optical frequencies and showing proper characteristics of blazars. Sources are classified as BL

[4]http://www.asdc.asi.it/bzcat

Lacertae objects (BZB), flat spectrum radio quasars (BZQ) or as blazars of uncertain type (BZU).

3.1. The Figure-of-Merit Method

The figure of merit (FoM) approach requires a large, uniform all-sky sample of radio sources from which to draw; for this purpose, we use the Combined Radio All-Sky Targeted Eight GHz Survey (CRATES; Healey et al. 2007) catalog. In order to quantify the correlation between CRATES sources and LAT detections, we compare the average number of positional coincidences between LAT sources and CRATES sources to the number of positional coincidences between LAT sources and sources drawn from 1,000 randomized simulations of the radio sky. We count as a positional coincidence any occurrence of a radio source (real or simulated) within twice the 95% error radius of a LAT source, and we generate the simulated radio skies by scrambling the Galactic coordinates of the CRATES sources while keeping their radio flux densities, spectral indices, and counterpart RASS fluxes intact.

We define the excess fractional source density of radio/γ-ray matches as $n = 1-(N_{\rm rand}/N_{\rm CRATES})$ and we compute this quantity in bins of radio flux density $S_{8.4}$ at 8.4 GHz, radio spectral index α, and X-ray flux F_X from the ROSAT All-Sky Survey (RASS; Voges et al. 1999). These functions—$n(S)$, $n(\alpha)$, and $n(F_X)$— constitute the counterpart spectral energy distribution (SED) components of the FoM. The final component is the dependence on the offset between the radio position and the LAT position, which we model simply as $n_{\rm pos} = 1 - {\rm CL}$, where CL is the confidence limit of the LAT localization contour passing through the radio position. The FoM is then given by $100 \times n(S) \times n(\alpha) \times n(F_X) \times n_{\rm pos}$. To evaluate the significance of the FoM, we again generated, in the manner described above, 1,000 random simulations of the radio sky and computed the average distribution of FoM. We compared this to the distribution of FoM for the real CRATES sky by again computing the excess fractional source density as a function of FoM. This fractional excess can be directly interpreted as a probability P_i of radio/γ-ray association for source i, giving an immediate mapping from FoM to association probability for each individual source (i.e., $1 - P_i$ is the probability of a false positive association). We find that 1,000 simulated skies result in sufficient statistics in each FoM bin to ensure that the mapping is robust. Very similar results are obtained with 10,000 simulations.

The results of this association procedure are shown in Table 1 and Table 2. Most of the associated radio sources are in the Candidate Gamma-Ray Blazar Survey (CGRaBS; Healey et al. 2008), an optical survey of the 1,625 CRATES sources that were most similar in their radio and X-ray properties to the 3EG blazars. Optical spectroscopy of the sources with unknown redshifts is ongoing. We also considered the possibility of an association with a non-CRATES radio source when no CRATES association was found. Indeed, a FoM can be computed for any object for which the necessary radio data are available. Thus, for those LAT sources without CRATES associations, we drew candidate counterparts from the 1.4 GHz NRAO VLA Sky Survey (NVSS; Condon et al. 1998) or the 843 MHz Sydney University Molonglo Sky Survey (SUMSS; Mauch et al. 2003), searched

NED for archival 8.4 GHz data, and calculated the FoM for each candidate. These procedures find high-confidence ($P > 0.90$) associations for 101 of the 125 non-pulsar sources in the 0FGL list with $|b| > 10°$ for an association rate of 81%. We also find low-confidence FoM associations ($0.40 < P < 0.90$) for 14 more sources, bringing the total association rate to 92%. Thus, the radio-bright blazar population continues to dominate the extragalactic sky.

The individual association probabilities can be used to estimate the number of false positives in a given sample: if the probabilities P_i are sorted from highest to lowest, then the number of false positives in a sample of k sources is $N_{\rm false} \approx \sum_{i=1}^{k} (1 - P_i)$. Among the high-confidence associations, there are ∼3 false positives, and less than one of the 74 most probable associations should be false.

We also studied the power of the FoM analysis to reject a blazar association for a LAT source. We considered NVSS/SUMSS sources in the direction of the unassociated LAT sources and computed the FoM that each source would have if (A) it were as bright as the 4.85 GHz flux density upper limit from the Green Bank 6 cm survey (GB6; Gregory et al. 1996) or the Parkes-MIT-NRAO survey (PMN; Griffith & Wright 1993) (unless the source had an actual GB6/PMN detection, in which case we used the measured flux density) or (B) its radio spectrum were as severely inverted as $\alpha = +0.75$ between 1.4 GHz and 4.85 GHz, whichever constraint was tighter. From the low-frequency radio spectrum (or upper limits), we extrapolated the implied 8.4 GHz flux density. If the resulting FoM indicated that the source could conceivably be a flat-spectrum blazar, then we drew no conclusion, but if we found that the "best-case" association probability were 0%, then we concluded that the LAT source was not associated with any typical member of the population of flat-spectrum blazars, and we refer to such cases as "anti-associations." Note that the spectral index $\alpha = +0.75$ is an extremely conservative cutoff. The most inverted radio spectrum for any actual association has $\alpha < 0.65$. We are able to secure anti-associations for 10 sources. In fact, five of these turn out to be high-latitude LAT pulsars and pulsar candidates. This shows that, given a reliable LAT error circle, the FoM analysis is capable of indicating definitively that a source is not a blazar

3.2. Summary of association results

The combination of the FoM (described above) and positional association methods yields a number of 106 high-confidence ($P \geq 0.90$) associations (constituting the LBAS) and 11 low-confidence (0.40< P <0.90) associations listed in Table 1 and 2 respectively. Simple extrapolation of these numbers implies that the LAT should be detecting some 20-25 blazars through the Galactic plane at $|b| < 10°$. Indeed, several have already been located, e.g. 0FGL J0036.7+5951 (1ES 0033+595), 0FGL J0730.4−1142 (PKS 0727−11), 0FGL J0826.0−2228 (PKS 0823−223), 0FGL J1802.6−3939 (PMN J1802−3940), 0FGL J1833.4−2106 (PKS 1830−211). A more complete search for Galactic background blazars, incorporating spectrum, variability and multiwavelength properties is in progress.

Tables 1 and 2 report, for each source, the LAT name, the name of the associated source based on the FoM method, the value of the FoM parameter and its probability, the name of the positionally associated source and its probability, the redshift and the AGN class. Fig. 4 shows the sky location of the LBAS AGNs.

One source, 0FGL J10340+6051 reported in Table 1, merits special comment. Two radio associations were found by the FoM method for this γ-ray source, one with very high probability and one with lower, but still significant, probability reported in Table 2. Although the high-probability source likely dominates the γ-ray emission, it is entirely plausible that the low-probability source contributes non-negligibly to the total γ-ray flux. We believe that as the LAT detects more sources and confusion of the γ-ray sky increases, the power of the FoM formalism will become increasingly important to the identification of multiple lower-energy counterparts of complex γ-ray sources.

Fig. 5 shows the overall, normalized angular separation distributions for both sets of sources (i.e. high- and low-confidence associations). The solid curve corresponds to the expected distribution (χ^2 distribution with 2 d.o.f.) for real associations, the dashed one for accidental associations. This figure provides confidence that most associations are real. From this figure, it appears that the 1.4 correction factor applied to the error radius is somewhat overestimated. This overly conservative factor will be significantly reduced with additional analysis updates.

Four new blazars were discovered. Two of these, CRATES J1012+2439, and CRATES J1032+6051 were classified as FSRQ blazars while CRATES J0144+2705 is a BL Lac. The classification of these three sources was made on the basis of the broad lines observed in their optical spectrum obtained after the LAT detection (Shaw et al., in preparation). The forth new LAT detected blazar is CLASS J1054+2210. Its classification as a BL Lac object was made possible by the analysis of its optical spectrum available at the SDSS on-line archive. As discussed above, CRATES J1032+6051 is the source which has a low probability to be associated with 0FGL J10340+6051.

The other sources listed in Table 1 and 2 were classified as FSRQ or BLLac following the *Roma*-BZCat and CRATES/CGRaBS catalogs. Some sources, which cannot be properly classified because of the scarcity of available data or which show optical spectra intermediate between those of BL Lacs, FSRQs or radio galaxies, were assigned to the "uncertain class" ("Unc" label in the tables).

Based on this classification, the LBAS comprises 57 FSRQs, 42 BL Lac objects, 5 blazars of uncertain type, and 2 radio-galaxies (RGs). The relevant *EGRET* sample of reference corresponds to that of the 18 month *EGRET* all-sky survey during Phase 1 of the CGRO mission (Fichtel et al. 1994; Dermer 2007). This survey had relatively uniform exposure, and contained 60 sources, 46 FSRQs, 14 BL Lacs. BL Lacs make up 40% of the LBAS blazars, a fraction significantly higher than found with *EGRET* (23%). The detection of hard sources (BL Lac objects, see below) by the LAT is intrinsically favored over soft ones (FSRQs). This is partly due to the strongly energy-dependent PSF. The larger bandpass and higher energy for the peak sensitivity (in the $\sim$ 1-5 GeV range) of the LAT as compared to *EGRET* adds to this effect.

Eleven LBAS sources are associated with blazars already detected in the TeV energy range by the ground based imaging air Cherenkov telescopes. Among these, 7 are classified as high-frequency peaked BL Lacs (HBLs): 1ES 1011+496, Mrk 421, PG 1553+11, Mrk 501, 1ES 1959+650, PKS 2005−489 and PKS 2155−304; 3 are low-frequency peaked BL Lacs (LBLs): 3C 66A, W Com and BL Lac and one is a FSRQ: 3C 279. These 11 sources represent more than 50% of the TeV blazars detected so far (21). The results of simultaneous observations that cover the optical, X-ray, and high energy gamma-ray bands (LAT and H.E.S.S.) of PKS 2155-304 are reported in Aharonian et al. (2009). Another three HBLs in the LBAS are not yet detected in the TeV range: KUV00311−1938, 1ES0502+675, B3 0133+388. A total of 10 HBLs are thus present in the LBAS, a remarkable feature given that sources in this class were difficult to detect in the GeV range. Many of these sources were not particularly flaring at other wavelengths during the period of observation.

We compared the broad-band (radio, optical, X-ray) properties of our sample of *Fermi*-LAT detected blazars with those of the known blazars listed in the *Roma*-BZCat catalog and found that the broadband properties of the *Fermi*-LAT detected BL Lacs and FSRQs are consistent with the parent population of FSRQs and BL Lacs. This is illustrated in Fig. 6 displaying the soft X-ray flux vs radio flux density (at 1.4 GHz) diagram for the Fermi-LAT blazars and the full blazar catalog.

The LBAS includes 13 sources (10 FSRQs and 3 BL Lacs) that were detected in a flaring state promptly announced to the community through Astronomical Telegrams. Among these, 0FGL J2254.0+1609, associated with 3C 454.3, is the brightest gamma-ray extra-galactic source observed in the 3-month *Fermi*-LAT survey and is studied in detail in Abdo et al. (2009a).

The *Fermi*-LAT has discovered gamma-ray emission from a source having an high-confidence association with NGC 1275, the supergiant elliptical galaxy at the center of the Perseus galaxy cluster. EGRET observations yielded only an upper limit to the NGC 1275 gamma-ray emission. All the details about the gamma-ray properties of this source will be reported in Abdo et al. (2009b).

Cen A is the nearest radio galaxy to us and it was one of the few radio galaxies associated with a 3EG source (J1324−4314; Sreekumar et al. 1999). It is included in the LBAS and the position of its nucleus is well inside the 95% confidence error radius of the source 0FGL J1310.6−4301. The measured *Fermi* flux is $F_{100} \simeq 2.3 \times 10^{-7}$ ph cm^{-2} s^{-1}, about a factor of 2 greater than that measured by *EGRET* (Sreekumar et al. 1999).

Recently, two more sources reported in the 3EG catalog were tentatively associated with radio galaxies, 3C 111 (Hartman et al. 2008), and possibly NGC 6251 (Mukherjee et al. 2002; Foschini et al. 2005). These objects are not LBAS sources but the number of radio-galaxies detected at high-energy is expected to increase in the near future as more data accumulate.

Table 4 lists the 33 sources associated with 3EG sources (two more located at $|b| < 10^\circ$ were also incorporated). Three bright EGRET blazars associated with 0827+243, PKS 1622−297 and 1730−130 (NRAO 530), whose average EGRET fluxes are in the range of (25 - 47) $\times 10^{-8}$ ph($E >$ 100 MeV) cm^{-2} s^{-1} do not appear in the LBAS. Presumably, these blazars are simply in a lower flux state than when EGRET was in operation. These 3 sources are also among the 22 sources in the pre-launch LAT monitored list[5]. Of these 22 sources, 17 have high-significance LAT detections in the first 3-months of data. The remaining two monitored sources (H 1426+428, 1ES 2344+514) did not have previous 3EG detections and thus were not expected to be very bright GeV sources.

We note that the LBAS object B2 0218+35 is a well-known gravitational lens. The source PMN J0948+0022, associated with 0FGL J0948.3+0019, has a flat radio spectrum, but shows an optical spectrum with only narrow emission lines, making it an "uncertain"-type object in the *Roma*-BZCat.

4. Gamma-ray properties of the LBAS

4.1. Introduction

Table 3 lists the key properties of the 116 sources associated with AGNs (sources with low-confidence associations are in italics): the name, equatorial and galactic coordinates, the TS parameter measuring the significance of the detection, the photon index (Γ), the photon flux F_{100}, the weekly peak flux, the photon flux F_{25} and the variability flag. The uncertainties are statistical only. From Table 3 (last column), 40 FSRQs (70%), 12 BL Lacs (29%) and 1 Uncertain blazar (0FGL J0714.2+1934) present in the LBAS show evidence for variability. The observed variability for FSRQs is thus higher than for BL Lacs. One must be careful in interpreting this result as the flux distributions are different for the two classes (see Fig. 7), making the detection of variability easier for FSRQs. An in-depth variability analysis of the LBAS is beyond the scope of this paper.

Table 4 gives similar parameters for the subset of 35 sources (including both high-confidence and low-confidence associations, plus two at $|b| < 10°$) corresponding to 3EG sources. This subset will be discussed in more detail in section 5.

The source photon index is plotted as a function of the flux in Fig. 7. It is already visible in this figure that the photon indices of BL Lac objects (open circles) and FSRQs (closed circles) are quite distinct. The flux sensitivity (calculated in the same way as for the map shown in Fig. 2 and depicted as solid lines for two different galactic latitudes) is fairly strongly dependent on the photon index. The upper envelope in the spectral index - flux (>100 MeV) plot reflects that the peak sensitivity of the LAT is at energies much higher than 100 MeV. These ranges of spectral index and apparent flux limits translate to approximately constant limits above 1 GeV. For a photon index of 2.2, the 10 σ flux sensitivity $F_{100} \simeq 5\times 10^{-8}$ ph cm^{-2} s^{-1}, about 3 times lower than that of the Third *EGRET* catalog.

---

[5]http://fermi.gsfc.nasa.gov/ssc/data/policy/LAT_Monitored_Sources.html

4.2. Flux

It makes sense to compare the LBAS fluxes with those reported in the Third EGRET Catalog for the EGRET sample. As several analyses (e.g. Mücke & Pohl 2000; Dermer 2007) used the peak flux (maximum flux in all EGRET viewing periods), instead of the mean flux because of the fairly non-uniform coverage in the EGRET Catalog, comparisons will be performed both for the mean and peak flux distributions. For *EGRET*, both distributions are biased as observations were preferentially made of sources known to be highly variable in the gamma-ray band, and some of the observations were triggered by ToO requests when an object was brightly flaring in other wavebands. No such bias exists for the LAT.

Fig. 8a compares the mean flux distribution measured in the LBAS with that measured in the *EGRET* sample. The high-flux ends of these distributions look similar. This observation points to a nearly constant global gamma-ray luminosity of detectable blazars at a given time, as can naively be expected. In stark contrast, the weekly peak flux distributions (Fig. 8b) look different, the peak fluxes being significantly higher in the *EGRET* sample. This feature probably arises from the shorter sampling period for the *Fermi*-LAT as compared to *EGRET*. In the 3-month period considered here, a given source had much less opportunity to explore very different states than in the 4.5 years over which the *EGRET* observations were conducted. Another illustration of this effect is given in Fig. 8c,d where the peak flux vs the mean flux and the peak flux/mean flux ratio distributions are shown respectively. The inference that the gamma-ray blazars have characteristic variability timescales of months to years is well confirmed by the observation that only $\simeq 30\%$ of the *EGRET* blazars are still detected by the LAT at a comparable flux.

4.3. Photon index

The photon index distribution gives insight into the emission and acceleration processes acting within the AGN jets, as it enables some of the physical parameters involved in these processes to be constrained. Moreover, it can be used to test whether the BL Lac and FSRQ populations have different $\gamma-$ray emission properties.

Fig. 9 top displays the photon index distribution for all the LBAS sources. This distribution looks fairly similar to that observed for the *EGRET* sample (Nandikotkur et al. 2007): it is roughly symmetric and centered at $\gamma = 2.25$. The corresponding distributions for FSRQs and BL Lacs are shown in Fig. 9 middle and bottom respectively. These distributions appear clearly distinct, with little overlap between them. This is a remarkable feature, given that the statistical uncertainty typically amounts to 0.1 for most sources. The distributions have (mean, rms)=(1.99, 0.22) for BL Lacs and (2.40, 0.17) for FSRQs. We used a Kolmogorov-Smirnov (KS) test to test the null hypothesis that both index samples are drawn from the same underlying distribution and found a probability of 2×10^{-12} [6]. Although indications for the existence of two spectrally distinct populations (BL Lacs and FSRQs) in the *EGRET* blazar sample were mentioned in the literature (Pohl et al. 1997; Venters & Pavlidou 2007), this is the first time that the distinction appears so clearly. The mean photon index of the 10 HBLs included in the LBAS is 1.76, i.e significantly lower (sources are harder) than the mean of the whole BL Lac subset as expected for these high-energy peaked sources.

To infer physical properties of the blazar populations from the observed photon index distributions, possible instrumental and/or statistical effects have to be assessed. A systematic bias may indeed arise in the likelihood analysis of sources with low photon statistics. To quantify this possible bias we performed a simulation study with the *gtobssim* tool which is part of the *ScienceTools*. This tool allows observations to be simulated using the instrument response functions and the real orbit/attitude parameters. Both instrumental and diffuse backgrounds were modeled on the basis of the real backgrounds observed by the LAT.

1. Samples of sources (100 FSRQs and 100 BL Lacs) with random positions in the $|b| > 10°$ sky were simulated.

2. The real spacecraft orbit and attitude profiles spanning 94 days starting from Aug 4 2008 were used.

3. The sources were assumed to have a power-law energy distributions. The photon index was drawn from a gaussian distribution with (mean, sigma)= (2.0,0.3) for BL Lacs and (2.3,0.3) for FSRQs. These distributions are referred to as "input" probability distribution functions (pdfs).

4. Fluxes were generated according to a lognormal distribution $f(x) = \frac{1}{x\sigma\sqrt{2\pi}} \exp \frac{-(\ln x - \mu)^2}{2\sigma^2}$ with $\mu = \ln 10^{-7}$ and $\sigma = 0.4$

5. A likelihood analysis was performed for all sources. The pdfs of the spectral indices and fluxes were built for sources with TS>100 ("like" pdfs). The TS cut was also applied to the "input" pdfs.

Possible bias arising from the likelihood analysis as well as the robustness of the separation between BL Lac and FSRQ "like " pdfs were studied by means of KS tests. "Input" and "like" pdfs were found to be consistent with a probability of 99.5%, 88.4% for BLLacs and FSRQs respectively, excluding any sizeable bias coming from the likelihood analysis. The TS cut was observed to only affect the distribution tails. Concerning the separation between BL Lacs and FSRQs, the KS test returned that the probability for the two distributions to result from the same parent distribution is 7×10^{-7}.

[6]We are aware of the fact that the KS test is not optimal for binned data, but it is accurate enough to reject the null hypothesis

5. Sources already detected by *EGRET*

After an elapsed time of about 10 years, it is interesting to look at the fraction of the AGNs that were active in the *EGRET* era and are detected again by the LAT with a comparable flux. Out of 116 sources in the *Fermi*-LAT sample, 3 sources have positions compatible with sources in the Third *EGRET* Catalog. Two additional sources, 0FGL J1802.6−3939 and 0FGL J1833.4−2106 located at $|b| < 10°$ fulfills this condition as well. The 35 sources are listed in Table 4, along with the mean fluxes and photon indices measured by the *Fermi*-LAT and *EGRET* as well as the AGN class. These 35 AGNs are composed of 20 FSRQs, 11 BL Lacs, 3 of uncertain type and 1 AGN (Cen A). The BL Lacs are again overrepresented (with a fraction of 31%) as compared to the 1st year sky survey *EGRET* sample (14 out of 60, i.e. 23%). The (non-simultaneous) fluxes and indices measured by both intruments are compared in Fig. 12. The large scatter observed when comparing the fluxes (Fig. 12 left) can be expected from the variable nature of the blazar emission. The scatter observed when comparing the photon indices is more moderate, as could be expected from the fairly strong correlation between photon index and blazar class mentioned above. For many sources, and most especially for BL Lacs, the indices are measured by the *Fermi*-LAT with a much better accuracy.

6. Radio gamma-ray connection

With 116/125 high $|b|$, non-pulsar LAT bright sources associated with radio sources in the CRATES/CGRaBS and the *Roma*-BZCAT lists, we confirm the findings of the 3EG catalog. In particular, 98/106 ($\sim 92\%$) of our high confidence associations have flux density above 100 mJy at 8.4 GHz. In terms of the radio luminosity $L_r = \nu L(\nu)$, the sources in the present sample with a measured redshift span the range $10^{39.09} < L_r < 10^{45.33}$ erg s^{-1}. As shown by the histogram in Fig. 13, BL Lacs and FSRQ are not uniformly distributed in this interval, with the former on average at lower radio luminosities ($\mathrm{Log}\, L_{r,\,\mathrm{BL\,Lacs}} = 42.8 \pm 1.1$ [erg s^{-1}]) than the latter ($\mathrm{Log}\, L_{r,\,\mathrm{FSRQ}} = 44.4 \pm 0.6$ [erg s^{-1}]). Blazars of uncertain type generally lack a redshift. Of the two radio galaxies associated with objects in the LBAS, NGC 1275 is similar to BL Lacs ($L_r = 10^{42.21}$ erg s^{-1}), while Cen A lies at the very lower end of the radio power distribution, with $L_r = 10^{39.09}$ erg s^{-1}.

Cen A, the source associated with 0FGL J1325.4−4303, is also the only source showing a significant amount of extended radio emission at low frequency ($S_{8.4}/S_{\mathrm{low}} = 0.005$). For all other sources with a low frequency (typically, 365 MHz from the Texas survey, 325 MHz from the WENSS, or 408 MHz from the B2) and a high frequency, high resolution (typically at 8.4 GHz from CRATES) flux density measurement, we find little or no evidence of significant deviation from $L_{\mathrm{low}} = L_{8.4}$. Therefore, we find not only that all the sources in our sample are radio emitters, but that they also possess compact cores with flat radio spectral index and much higher luminosity than those of radio galaxies of similar or larger power (Giovannini et al. 1988).

Thanks to the comparatively large number of LBAS sources, it is worthwhile to perform a statistical comparison of their properties in the gamma-ray and radio bands. Previous studies based on EGRET data for 38 extragalactic point sources have been reported (Mücke et al. 1997), which did not support claims of correlations between radio and gamma-ray luminosities. In particular, the analysis of possible correlations needs to be treated with care, because of the many biases that can arise, e.g. from the common redshift dependence when one considers luminosities, or from the reduced dynamical range when one considers mean flux densities, just to name a few.

We have therefore looked at several possible pairs of observables, and we summarize our results in Table 5. In general, we apply the K-correction to the luminosities but not to the fluxes, since this would introduce a bias for the sources without a known redshift. We show in Fig. 14 (left panel) the peak gamma-ray flux $S_{E>100\,\mathrm{MeV}}$ vs the radio flux density $S_{8.4\,\mathrm{GHz}}$ from CRATES (or NED, in the few cases in which the source is not in the CRATES list). In general, BL Lacs tend to populate the low flux region, and FSRQs the high flux region. Such a constellation is prone to create correlations artificially from purely combining both populations. Given their different redshift distributions, this would be even more apparent in the luminosity plane. For this reason, it is necessary to consider the two populations separately (see Table 5). Indeed, the results of our analysis show the significance of a radio-to-gamma-ray connection to be marginal at most on the basis of the present data, in particular for the FSRQs. Clearly, there is need for a deeper analysis on an enlarged sample regarding this issue, including Monte-Carlo simulations, which we defer to a forthcoming paper.

Finally, we show in the right panel of Fig. 14 the radio luminosity vs. gamma-ray spectral index plane. Thanks to the large LAT energy range, the separation between BL Lacs and FSRQs is readily seen, showing a trend of softer spectral indices for more luminous radio sources. Moreover, this plot seems quite effective at finding sources of a different nature, such as the radio galaxy Cen A, whose gamma-ray index is much softer than that of other low power radio sources. For instance, 0FGL J00174−0503 is a FSRQ at $z = 0.227$ (Healey et al. 2008) with index = 2.71 and radio luminosity $L_r = 10^{42.36}$ erg s^{-1}, which could then be a rare case of low-energy peak and low radio luminosity blazar. The other source with large photon index (2.60) and comparatively low radio luminosity ($L_r = 10^{43.22}$ erg s^{-1}) is associated with the peculiar source PMN J0948+0022.

7. Population Studies

As described before, the LBAS includes 57 FSRQs, 42 BL Lac objects, 5 blazars of uncertain type and 2 radio galaxies. Ten other sources have lower confidence associations with known blazars. This sample is already comparable with that provided by EGRET and can be used to derive some *early* results about the redshift and source count distributions and the luminosity function of blazars.

7.1. Redshifts

Fig. 15 and Fig. 16 display the redshift distributions for FSRQs and BL Lac objects, respectively, and their comparison with those of the parent distributions in the BZCat catalog. Please note that 12 of 42 BL Lacs have no measured redshifts. BL Lac objects are generally found at low, $z \lesssim 0.5$, redshift, whereas the peak of the FSRQ redshift distribution is around $z \cong 1$. Similar distributions were observed for the *EGRET* blazars (Mukherjee et al. 1997). In the future, as fainter sources become visible, detection of additional nearby radio-galaxies will enhance the number of very low redshift objects in the AGN redshift distributions measured with the *Fermi* LAT.

Fig. 17 shows the luminosities of the detected sources plotted as a function of their redshifts. The isotropic gamma-ray luminosity L_γ was derived using:

$$L_\gamma = 4\pi S d_L^2/(1+z)^{1-\alpha}\,. \tag{1}$$

Here, S is the γ-ray energy flux (E > 100 MeV), α is the energy index and d_L is the luminosity distance. A beaming factor $\delta = 1$ was assumed. The solid curve corresponds to a flux limit of $F_{100} = 4 \times 10^{-8}$ ph cm^{-2}s^{-1}.

7.2. log N - log S

7.2.1. Monte Carlo Simulations

Proper population studies must rely on a thorough understanding of the properties of the survey where these objects have been detected. In order to properly estimate the source-detection efficiency and biases, we performed detailed Monte Carlo simulations. The method we adopted is the one developed for ROSAT analysis (Hasinger et al. 1993) and lately used (Cappelluti et al. 2007) for the analysis of the XMM-COSMOS data. For each source population (blazars, FSRQs and BL Lacs) we created a set of >20 LAT all-sky images with background patterns resembling as close as possible the observed ones. The simulations were performed using a similar method as that described in section 4.3. An extragalactic population of pointlike sources was added to each simulated observation. The coordinates of each source were randomly drawn in order to produce an isotropic distribution on the sky. Source fluxes were randomly drawn from a standard log N–log S distribution with parameters similar to the one observed by LAT (see next section). Even though the method we adopt to derive the survey sensitivity does not depend on the normalization or the slope of the input log N–log S, using the real distribution allows us to produce simulated observations which closely resemble the real LAT sky. The photon index of each source was also drawn from a Gaussian distribution with observed mean and $1\,\sigma$ width consistent with the real population. Thus, for the three simulation sets we adopted the following photon indices similar to the measured ones:

- 2.24±0.25 for the total blazar population;

- 2.41±0.17 for the FSRQ population;
- 1.98±0.22 for the BL Lac population.

More than 30000 sources were simulated for each population. The mock observations were processed applying the same filtering criteria used for real in-flight data. Source detection was performed on E>200 MeV photons with a simplified version of the detection algorithm[7]. For every pair of input-output sources, we computed the quantity:

$$R^2 = \left(\frac{x - x_0}{\sigma_x}\right)^2 + \left(\frac{y - y_0}{\sigma_y}\right)^2 + \left(\frac{S - S_0}{\sigma_S}\right)^2 \qquad (2)$$

where x, y and S are the source coordinates and flux of the detected sources while x_0, y_0 and S_0 are the corresponding values of the input sources and σ_x, σ_y, σ_S the associated statistical uncertainties. We then flagged those with the minimum value of R^2 as the most likely associations. Only sources at $|b| \geq 10°$ are retained.

The goal of these simulations is to derive the probability of detecting a source (with given mean properties, e.g. photon index and flux) in the LAT survey as a function of source flux. This can be computed from the simulations reported above as the ratio between the number of detected and input sources in a given flux bin. The detection efficiencies for the three source populations are reported in Fig. 18. A few things can be noted readily. First, the bias of the LAT survey against soft sources (i.e. FSRQs) is apparent. Second, the LAT $|b| \geq 10°$ survey becomes *complete* for F(>100 MeV)$\geq 2\times10^{-7}$ ph cm^{-2} s^{-1} irrespective of the source photon index or its location in the sky. Multiplying these functions by the solid angle Ω of the survey (34089.45 deg^2 in case of a $|b| \geq 10°$ cut) yields the so called sky coverage which is used for the statistical studies reported in the next sections.

7.2.2. Incompleteness of the Extragalactic Sample

We report in Table 6 the composition of the $|b| \geq 10°$ sample. The number of sources with high-confidence associations is 106. Of these 57 are FSRQs and 42 are BL Lacs. As already shown in the previous sections, FSRQs and BL Lacs are represented in almost equal fractions in the LAT survey. The 5 blazars with uncertain classifications are likely split between these two categories as the redshift-luminosity plane (Fig. 17) shows. The incompleteness factor varies as a function of the sample under study. When considering the non-pulsar part of the high-confidence sample, the incompleteness is given by low confidence and unassociated objects. This turns out to be ∼11 %. However, when considering the FSRQ and BL Lac samples separately one must also include the

[7]The complexity of the official detection algorithm makes it virtually impossible to apply it to a large number of data sets. We tested on real data that, for the scope of this investigation, our simplified detection algorithm produces results consistent with more elaborate ones.

sources with uncertain classifications. Thus the incompleteness factor of the FSRQ and BL Lac samples rises to ∼15 %. A reasonable and simple hypothesis is one which assumes that these sources reflect the composition of the identified portion of the sample. This would mean that there are an additional ∼9 FSRQs and ∼7 BL Lacs are hiding among the unidentified/unassociated/low-confidence sources. These uncertainties will be used in the next sections.

Since the uncertainty due to the incompleteness is relatively large, we will use a *flux-limited* sample to verify the results derived from the main sample. Indeed, for $F_{100} \geq 1.25 \times 10^{-7}$ ph cm^{-2} s^{-1} the number of uncertain, unassociated, and low-confidence sources falls to 2 (and 2 are anti-associated). Above this flux limit, the sample contains 44 sources of which 29 and 9 are FSRQs and BL Lacs respectively, while 2 are Radio galaxies. Moreover, all but one BL Lac have a measured redshift. Thus, while low numbers penalize this *flux-limited* sample, its incompleteness is <5 %.

7.2.3. Source Counts Distributions

The source counts distribution, also known as the log N–log S, flux, or size distribution, is readily computed once the sky coverage is known through the expression:

$$N(>S) = \sum_{i=1}^{N_S} \frac{1}{\Omega_i} \mathrm{deg}^{-2}, \tag{3}$$

where N_S is the total number of detected sources with fluxes greater than S, and Ω_i (i.e. Fig. 18 multiplied by the solid angle) is solid angle associated with the flux of the *ith* source. The variance of the source number counts is defined as

$$\sigma_i^2 = \sum_{i=1}^{N_S} \left(\frac{1}{\Omega_i} \right)^2 . \tag{4}$$

In building the source counts distributions, we used the source flux averaged over the three month timescale. The log N–log S of the entire extragalactic sample (excluding pulsars) is shown in Fig. 19.

We fitted the source counts distribution with a power-law model of the type:

$$\frac{dN}{dS} = n(S) = A \left(\frac{S}{10^{-7}} \right)^{-\alpha} . \tag{5}$$

A common practice in this case (e.g., see Ajello et al. 2008) is to fit the unbinned dataset employing a maximum likelihood (ML) algorithm. For this purpose the ML estimator can be written as

$$\mathcal{L} = -2 \sum_i \ln \frac{n(S_i)\Omega(S_i)}{\int n(S)\Omega(S) dS} , \tag{6}$$

where i runs over the detected sources. The $1\,\sigma$ error associated to the fitted parameters (in this case α) is computed by varying the parameter of interest, while the others are allowed to float, until an increment of $\Delta\mathcal{L}$=1 is achieved. This gives an estimate of the 68 % confidence region for the parameter of interest (Avni 1976). In this formulation of the ML function, the normalization A is not a parameter of the problem. Once the slope α is determined, the normalization is derived as the value which reproduces the number of observed sources. An estimate of its statistical error is given by the Poisson error of sources used to build the log N–log S.

Since the sky coverage is somewhat uncertain at very low fluxes, the fit is performed above F(>100 MeV)= 7×10^{-8} ph cm^{-2} s^{-1} even though all the data are displayed. The results of the best fits to the different source counts distributions are summarized in Table 7. It is clear that all distributions are compatible, within their errors, with a Euclidean distribution ($\alpha = 2.5$). In order to check the stability of our results we have shifted the sky coverage of Fig. 18 by 20 % on either side. Taking the whole extragalactic population as an example (see first line of Table 7) we get that the best fit values of the slope are 2.47 and 2.62 for the −20 % and +20 % case respectively. These values are consistent within the error (e.g. 2.59±0.12), showing that at bright fluxes our analysis does not suffer from major systematic uncertainties in the sky coverage. The same result holds for the other log N–log S distributions reported in Table 7.

The log N– log$S$ distributions for FSRQs and BL Lacs are shown in Fig. 20 and 21. We do not find any indication of a break in the source counts distributions of the two populations. As the fitting results of Table 7 show, there might be an intrinsic difference between the log N–log S of both populations, with the source counts distribution of BL Lacs being flatter than that of of FSRQs. However, both of them are compatible within 1 σ errors with the Euclidean value of 2.5. Moreover, the analysis of the *flux-limited* sample (see bottom part of Table 7) confirms the results of the main sample, showing that incompleteness is not a main issue in this study.

For the *EGRET* sample, a surface density for $F_{100} \geq 10^{-7}$ ph cm^{-2} s^{-1} of FSRQs and BL Lacs of 3.31 sr^{-1} and 0.83 sr^{-1}, respectively, is reported (Mücke & Pohl 2000). From LAT we derive that the surface density (above $F_{100} \geq 10^{-7}$ ph cm^{-2} s^{-1}) of FSRQs and BL Lacs is 4.41±0.72 sr^{-1} and 1.01±0.17 sr^{-1} respectively. Thus the LAT results are in good agreement with *EGRET*.

A measurement of the number fluence using the average three-month fluxes of bright *Fermi* blazars of different classes is readily obtained from the log N–log S distributions through the expression:

$$F_{diffuse} = \int_{f_{min}}^{f_{max}} \frac{dN}{dS}\ S\ dS\ . \tag{7}$$

Unless otherwise stated, we adopt a value for f_{min} of $4{\times}10^{-8}$ ph cm^{-2} s^{-1}. To compare with the *EGRET* results, the upper limit of integration cannot be set to infinity. Indeed, all point sources detected above $F_{100} \sim 10^{-7}$ ph cm^{-2} s^{-1} in the Second EGRET Catalog (2EG; Thompson et al. 1995) were subtracted in the measurement of the extragalactic diffuse γ-ray background (EDGB) (Sreekumar et al. 1998). Thus, we set f_{max} to 10^{-7} ph cm^{-2} s^{-1}. The integral in Eq. 7 yields a total flux of $1.06(\pm0.09){\times}10^{-6}$ ph cm^{-2} s^{-1} sr^{-1} This can be compared with the intensity of the EDGB, as measured by *EGRET*, of $1.45{\times}10^{-5}$ ph cm^{-2} s^{-1} sr^{-1}. Already in this small flux range, LAT is resolving into pointlike sources ∼7 % of the *EGRET* EDGB. Preliminary analysis of the log N–log S distributions shows that LAT is expected to resolve a much larger fraction of the EDGB within the next few months of observation.

7.3. Evolution of Blazars

7.3.1. Evolutionary Test

A simple and robust test of evolution is the $V/V_{\rm MAX}$ test Schmidt (1968). The quantity $V/V_{\rm MAX}$ is the ratio between the (comoving) volume within which the source has been detected and the maximum comoving volume available for its detection. For a given source, $V/V_{\rm MAX}$ is expected to be uniformly distributed between 0 and 1. For a population uniformly distributed in Euclidean space (and with constant properties with z) and non-evolving, the average $V/V_{\rm MAX}$ should be consistent with a value of 0.5. The error on the average value is $\sigma = 1/(12N)^{1/2}$ for N sources. A value of $<V/V_{\rm MAX}> > 0.5$ indicates positive evolution (more sources or brighter sources at earlier times), and the opposite indicates negative evolution.

The comoving volume for a *ith* source is given by

$$V = \int_{z=0}^{z=z_i} \frac{dV}{dz}\ \Omega(L_i, z) dz, \tag{8}$$

where dV/dz is the comoving volume element per unit redshift and unit solid angle (see e.g. Hogg 1999) and $\Omega(L_i, z)$ is the aforementioned sky coverage for the source with rest-frame luminosity L_i at redshift z. We note that the definition of the $V/V_{\rm MAX}$ reported in Eq. 8 encompasses also the definition of the V_e/V_a test (Avni & Bahcall 1980), which for the purposes here are formally equivalent.

We computed the average $<V/V_{\rm MAX}>$ for FSRQs, BL Lacs and all sources in the high-confidence sample with measured redshift (these includes the sources with uncertain classification). The results are summarized in Table 8. All 57 FSRQs present in the extragalactic sample (see Table 6) have a measured redshift. The $V/V_{\rm MAX}$ shows that the population of FSRQs detected by LAT evolves positively (i.e. there were more FSRQs in the past or they were more luminous) at the $3\,\sigma$ level. This result is also confirmed by the analysis of the 29 FSRQs which constitute a *flux-limited* sample (see lower part of Table 6).

Only 31 out of the 42 BL Lac objects have a measured redshift. The $V/V_{\rm MAX}$ test is compatible within $\sim 1\sigma$ with no evolution. Assigning the mean redshift value of the BL Lac sample (i.e. $\langle z\rangle$=0.38) to those objects without a without a redshift produces a value of $\langle V/V_{\rm MAX}\rangle$=0.472±0.046. The result does not change if the redshift is drawn from a Gaussian distribution with mean and dispersion consistent with the observed redshift distribution of BL Lacs. However, it is difficult to assess the validity of both these hypotheses. Indeed, the fact that these objects show a featureless continuum might suggest that their redshifts could be the largest in the sample (Padovani et al.

2007). In this case, their true redshift would produce a larger value of the $V/V_{\rm MAX}$ statistic. The $V/V_{\rm MAX}$ of all the objects with a measured redshift in the high-confidence sample is compatible with no evolution.

7.3.2. Luminosity Function of FSRQs

We estimate the gamma-ray luminosity function (GLF) in fixed redshift bins using the $1/V_{MAX}$ method (equivalent in our formalism to the $1/V_a$ method). For each bin of redshift the GLF can be expressed as

$$\Phi(L_\gamma, z) = \frac{dN}{dL_\gamma} = \frac{1}{\Delta\ L_\gamma}\sum_{i=1}^{N}\frac{1}{V_{MAX,i}} \tag{9}$$

where $V_{MAX,i}$ is the maximum comoving volume associated with the i_{th} source (see Eq. 8). The cumulative and differential luminosity functions of FSRQs, in three redshift bins, are reported in Fig. 22. One thing is readily apparent from this figure. FSRQs are strongly evolving. A non-evolving population would have GLFs which are continuous across different redshift bins. In the case of FSRQs we note a change in space density (or luminosity) with redshift. Also, one can see that the space density of intermediate-luminosity FSRQs (e.g. $L_\gamma \sim 10^{47}$ erg s^{-1}) is increasing with redshift. On the other hand, the most luminous FSRQs have an almost constant space density with redshift. This might be a sign of a cut-off in the evolution of FSRQs. A decline in the space density of luminous FSRQs has also been determined at radio and X-ray energies (e.g., Wall et al. 2005; Padovani et al. 2007; Ajello et al. 2009). We derive from the GLF that the space density of FSRQs with $L_\gamma > 7 \times 10^{45}$ erg s^{-1} is 1.05±0.13 Gpc^{-3}.

We made a Maximum Likelihood fit to the three unbinned datasets using a simple GLF model defined as

$$\Phi(L_\gamma, z) \propto L_\gamma^{-\beta}\ . \tag{10}$$

The ML estimator can be expressed similarly to Eq. 6 by the expression

$$\mathcal{L} = -2\sum_i \ln\frac{\Phi(L_{\gamma,i}, z_i)V(L_{\gamma,i}, z_i)}{\int \Phi(L_\gamma, z)V(L_\gamma, z)dL_\gamma}\ . \tag{11}$$

The results of the ML fits to the GLF of FSRQs are summarized in Table 9. For z ≥ 1, the GLF can be successfully parametrized by a single power-law model. The slope is compatible with the canonical value of 2.5–2.8 determined for X–ray selected samples of radio-quiet AGNs (Ueda et al. 2003; Hasinger et al. 2005; Silverman et al. 2008). This indicates that at high redshifts the *Fermi*-LAT is sampling the bright end of the luminosity distribution of FSRQs. For $z \leq 1$, the best-fit value of the slope β is 1.56±0.10, compatible with luminosity function slopes found in radio/X-ray selected samples (Padovani et al. 2007). This is much flatter than the canonical value of $\beta = 2.5$. As the cumulative GLF shows (left panel of Fig. 22), there might be a hint of a break with respect to a simple power-law model in the GLF. A more detailed analysis, comparing different methods to derive the GLF and its evolution, will be considered in future publications.

7.3.3. *Luminosity Function of BL Lacs*

The luminosity function of BL Lacs, reported in Fig. 23, is in agreement with the results of the $V/V_{\rm MAX}$ test. Indeed, sub-dividing the entire BL Lac sample in two bins of redshift produces two GLFs which connect smoothly to each other. A simple power-law GLF describes the entire dataset well. The GLF slope is $\beta = 2.17 \pm 0.05$ and is well in agreement with the value of 2.12±0.16 reported for a radio/X–ray selected sample of BL Lacs (Padovani et al. 2007). The GLF of 12 EGRET BL Lac objects in a recent study (Bhattacharya et al. 2008) was found to show no significant evidence for evolution, with a GLF slope $\beta = 2.37 \pm 0.3$. Past claims (e.g., Rector et al. 2000; Beckmann et al. 2003) of negative evolution of BL Lac objects, selected mainly in the X–ray band, are not confirmed by our data. The dynamical range of the LAT GLF samples 4 decades in luminosity and nearly 8 in space density. From our GLF we derive that the density of BL Lac objects with $L_\gamma > 3\times10^{44}$ erg s^{-1} is $1.9(\pm0.4)\times10^{-7}$ Mpc^{-3}.

Above a luminosity of $L_\gamma \sim 10^{47}$erg s^{-1}, the cumulative density of BL Lacs and FSRQs is comparable, with BL Lacs being $\sim$ 3 times less numerous than FSRQs. However, given the fact that they reach lower luminosities, BL Lacs are $\sim$ 200 times more abundant than FSRQs above their respective limiting luminosities.

8. Discussion

The value TS > 100 defining the detection significance for bright sources corresponds to $\gtrsim 10\,\sigma$ significance, or a limiting flux over the entire high-latitude sky of $\approx (3 - 10) \times 10^{-8}$ ph(> 100 MeV) cm^{-2} s^{-1} during the three-month sky survey. In comparison, *EGRET* reached a 5σ high-confidence on-axis flux limit of $\approx 15 \times 10^{-8}$ ph(> 100 MeV) cm^{-2} s^{-1} for a two-week pointing over ≈ 0.5 sr of the sky, only becoming complete at S $F_{100} \approx 25 \times 10^{-8}$ ph (cm^{-2} s^{-1} (Dermer 2007). Of the 66 high-confidence and 27 lower-confidence AGN associations in the 3EG catalog (Hartman et al. 1999), 32 sources in the *Fermi*-LAT sample were also detected with *EGRET*. An additional source is detected at $|b| < 10°$. Many of the other high-confidence *EGRET* sources are detected with *Fermi*-LAT at $TS < 100$, reflecting the rapid variability and periods of activity of γ-ray blazars on timescales of years or longer.

During the 18-month *EGRET* all-sky survey when exposure to all parts of the sky was relatively uniform compared to the remainder of the mission, 60 high-confidence blazars consisting of 14 BL Lacs and 46 FSRQs were found (Fichtel et al. 1994). Compared with $\approx$ 23% of *EGRET* blazars being BL Lac objects, nearly 40% of the *Fermi*-LAT blazars are BL Lac objects. The larger fraction of BL Lac objects in the *Fermi* bright AGN sample is partly a consequence of the good sensitivity to high-energy emission by *Fermi*-LAT, whereas self-vetoing in *EGRET* reduced its effective area to photons with energies $\gtrsim 5$ GeV(Thompson et al. 1993). Consequently, dim hard-spectrum sources are favored to be detected with the *Fermi*-LAT compared to *EGRET*.

A clear separation between the spectral indices of FSRQs and BL Lacs is found in the *Fermi*-LAT data (Fig. 9), with mean photon indices of $\Gamma = 2.40 \pm 0.17$ (rms) for FSRQs and $\Gamma = 1.99 \pm 0.22$ (rms) for BL Lac objects. A KS test gives a probability of 2×10^{-12} for the two index samples to be drawn from the same parent distribution. Moreover, the SEDs of bright flaring blazars in the cases of 3C 454.3 and AO 0235+164 show a spectral softening at $E \gtrsim 2$ GeV. If this behavior persists in weaker FSRQs, then an even greater fraction of BL Lac objects will be found in *Fermi*-LAT analyses over longer times, because signal-to-noise detection significance for weak hard-spectrum sources becomes better than for weak soft-spectrum sources due to the reduced background at higher photon energies.

Another reason for the larger fraction of BL Lac objects in the *Fermi*-LAT blazars could be related to the redshift distribution of the bright AGNs. The BL Lac objects are dominated by low-redshift, $z \lesssim 0.5$ blazars, with a tail extending to $z \approx 1$, whereas the FSRQs have a broad distribution peaking at $z \approx 1$ and extending to $z \approx 3$ (see Fig. 15 and Fig. 16). These distributions are similar to the distribution of *EGRET* blazars (Mukherjee et al. 1997). Because the peak of the *EGRET* FSRQ redshift distribution is already at $z \approx 1$, detection of higher redshift FSRQs with the more sensitive *Fermi*-LAT would be impeded by cosmological factors that strongly reduce the received fluxes. Moreover, the period of dominant AGN activity was probably at $z \approx 1$ or 2. The increased sensitivity for the BL Lac objects with *Fermi*-LAT, on the other hand, allows it to probe beyond the low-redshift population of BL Lac objects detected with *EGRET* where the detectable volume is still rapidly increasing with z. The likelihood of detecting $z \approx 1$ BL Lac objects does depend, however, on their evolution.

The simplest index of population evolution is the V/V_{MAX} test. We found $\langle V/V_{MAX} \rangle = 0.43 \pm 0.055$ for the BL Lac objects with redshift in the LBAS (Table 8), so that the BL Lac objects are within $\approx 1\sigma$ of showing no evidence for evolution. For the FSRQs in the LBAS, by contrast, we found $\langle V/V_{MAX} \rangle = 0.64 \pm 0.04$, so that the FSRQs exhibit strong positive evolution. The strong positive evolution of FSRQs and weakly negative or no evolution of BL Lac objects in the LBAS is contrary, however, to our reasoning that population evolution of the lower redshift BL Lac objects explains the larger fraction of BL Lacs in the LBAS compared with the BL Lac fraction observed with EGRET. As indicated by the indices of the $\log N - \log S$ (eq. 6 and Table 7), which show much weaker evidence for evolution than given by the V/V_{MAX} test, the actual situation may be more complicated and depend on both density and luminosity evolution.

The BL Lac objects are found to display systematically harder spectra, with νF_ν spectra rising at GeV energies, compared to the powerful FSRQs where the peak of the νF_ν spectrum is at photon energies $\lesssim 100$ MeV – GeV. This is generally attributed to a different dominant radiation process; self-Compton scattering of the jet electron's synchrotron emission in the case of BL Lac objects, and Compton scattering of external radiation fields in the case of FSRQs if leptonic processes dominate the radiation output (recently reviewed in Böttcher 2007). The excellent sensitivity and full-sky coverage of the *Fermi* LAT is, for the first time, giving us broadband evolving SEDs from the radio to the γ-ray regime in sources like 3C 454.3, PKS 2155-304, and others that will require detailed spectral modeling to assess the relative importance of self-Compton and external Compton scattering processes in the different blazar classes.

Such results will be important to determine whether FSRQs and BL Lac objects may have a direct evolutionary relationship, or instead represent separate unrelated tracks of supermassive black hole fueling and growth. A scenario whereby BL Lac objects are the late stages of FSRQs, as the gas and dust produced in a galaxy merger or tidal interaction fuels the supermassive black hole (Böttcher & Dermer 2002; Cavaliere & D'Elia 2002), provides a framework to understand the blazar phenomenology and makes definite predictions about the relative black hole masses in the two classes. The more abundant scattered radiation and fueling in the evolution from FSRQ to BL Lac object would then lead to a blazar sequence like behavior (Fossati et al. 1998; Ghisellini et al. 1998) if the amount of accreting matter controls black hole power and the surrounding radiation field.

It is still premature to compare the number of blazars in this bright source list with prelaunch predictions (Mücke & Pohl 2000; Stecker & Salamon 2001; Narumoto & Totani 2006; Dermer 2007; Inoue & Totani 2008) made on the basis of differing assumptions, to sensitivities $\approx 5\sigma$ rather than 10σ, and over different spans of time. Nevertheless, nearly complete surveys with far more sources than detected with *EGRET* are now available for calculating luminosity and number evolution, with implications that can be compared with results from the *EGRET* era.

This study can be used to examine the observational basis for assuming an underlying radio/γ-ray connection used to calculate the blazar contribution to the γ-ray background (Stecker & Salamon 1996; Giommi et al. 2006; Narumoto & Totani 2006). Figure 14 shows that except for a (at most) weak correlation of the brightest γ-ray blazars with the most radio-bright blazars, the γ-ray and radio fluxes display a large amount of scatter. Whether a stronger correlation can be found by comparing mean γ-ray fluxes with radio fluxes will require further study. But even at this early stage of the *Fermi* mission, we find that the bright sources can already comprise about 7% of the diffuse extragalactic γ-ray background flux measured with *EGRET* (Sreekumar et al. 1998).

We conclude this study by noting that the *Fermi*-LAT results imply the non-thermal luminosity density of AGNs on various size scales. A γ-ray blazar makes a contribution to the non-thermal emissivity $\propto L/V$ in terms of γ-ray luminosity L_γ and injection volume V derived from redshift. The *Fermi*-LAT results from Table 2 show that BL Lac objects provide local emissivities $\ell_{BL} \gtrsim 10^{31}$ W Mpc^{-3}, whereas FSRQs have $\ell_{FSRQ} \approx 10^{30}$ W Mpc^{-3}. Cen A, because of its proximity at $d \cong 3.5$ Mpc, dominates the non-thermal luminosity, with $\ell_{CenA} \approx 3 \times 10^{31}$ W Mpc^{-3} (Dermer et al. 2008). Sources of UHECRs must have a luminosity density within the GZK radius, ≈ 100 Mpc, of $\ell_{UHECR} \approx 3 \times 10^{29}$ W Mpc^{-3} or $\ell_{UHECR} \approx 10^{44}$ ergs Mpc^{-3} yr^{-1} (Waxman & Bahcall 1999). To have sufficient emissivity within the GZK radius, if AGNs are the sources of the UHECRs (The Pierre AUGER Collaboration et al. 2007), the *Fermi*-LAT results would therefore seem to favor BL Lac objects over FSRQs as the source of the UHECRs.

9. Summary

We have presented a list of 116 bright, $\gtrsim 10\sigma$ sources at $|b| \geq 10°$ taken from the list of bright sources (Abdo et al. 2009c) observed with the *Fermi*-LAT in its initial three-month observing period extending from August 4 to October 30 of 2008. Of these sources, 106 are associated with blazars with high confidence and compose the LBAS. The number of low-confidence AGN associations is 11 (one source having two possible associations - one high and one low confidence). At $|b| \geq 10°$, 5 sources out of a total of 125 non-pulsar sources remain unidentified. Two of the AGNs are associated with radio galaxies. The purpose of this work is to present the key properties of the AGN population of this bright GeV source list. The main results are summarized as follows:

1. With a $\sim 90\%$ success rate from correlating the bright gamma-ray source list with AGN radio catalogs (CRATES/CGRABS, BZCAT) the bright extragalactic gamma-ray sky continues to be dominated by radio-bright AGNs.

2. The number of HBLs in the LBAS detected at GeV energies (even when not flaring) has risen to at least 10 (out of 42 BL Lacs) as compared to one (out of 14 BL Lacs) detected by *EGRET*. Seven LBAS HBLs are known TeV-blazars.

3. Only $\sim 30\%$ of the bright Fermi AGN list were also detected by *EGRET*. This may be a consequence of the duty cycle and variability behavior of GeV blazars.

4. BL Lac objects make up almost half of the bright Fermi AGN sample (consisting of 57 FSRQs, 42 BL Lac objects, 2 radio galaxies, and only 5 AGN remain unclassified), while the BL Lac fraction in the 3EG catalog was only $\sim 23\%$. This feature most probably arises from the different instrument responses of the LAT and *EGRET*.

5. The mean flux distribution of the *Fermi* AGN remains similar to the corresponding one based on the *EGRET* sample, while the peak flux distributions differ appreciably.

6. We find a spectral separation between BL Lacs and FSRQs in the GeV gamma-ray band with FSRQs having significantly softer spectra than BL Lac objects. This confirms earlier indications for the existence of spectrally distinct populations in the *EGRET* blazar sample. The average photon index is 1.99 ± 0.22 (rms) for BL Lacs, with a tendency of HBLs displaying even harder spectra, and 2.40 ± 0.17 (rms) for FSRQs. A KS test gives a probability of 2×10^{-12} for the two index samples to be drawn from the same parent distribution.

7. *Fermi* FSRQs in the bright source list are on average more luminous and more distant than the *Fermi*-detected BL Lac objects in that list. I.e., FSRQs exhibit a broad redshift distribution, starting with $z = 0.158$ (3C 273), peaking at $z \approx 1$ and extending up to $z \approx 3$ while BL Lacs are mostly found in the ~ 0.1 redshift bin with a tail extending up to $z \approx 1$. No significant relation between the gamma-ray photon index and redshift is found within each source class, in agreement with corresponding studies based on the *EGRET* AGN samples.

8. The peak gamma-ray flux is at best only weakly related to the 8.4 GHz radio flux, with the brightest gamma-ray AGNs having the largest radio flux densities.

9. Using mean fluxes the Log N-Log S distribution of all the bright sources (except the pulsars) appears compatible with an Euclidean distribution without any breaks. This is also true within 1σ for the source counts distributions of the FSRQ and BL Lac sample separately. Surface densities of 4.28 ± 0.72 sr^{-1} and 1.01 ± 0.17 sr^{-1} ($F_{100} \geq 10^{-7}$ph cm^{-2} s^{-1}) for FSRQs and BL Lacs, respectively, are reached.

10. The combined emission in the flux range $F_{100,\mathrm{mean}} \approx (7-10) \times 10^{-8}$ph cm^{-2} s^{-1} observed from these individually resolved AGN during this three-month period already corresponds to $\sim 7\%$ of the *EGRET* detected extragalactic diffuse gamma-ray background.

11. A V/V_{max} analysis shows positive evolution at the 3 σ level for the bright *Fermi*-detected FSRQs with the most luminous FSRQs having an almost constant space density with redshift, while for the *Fermi*-detected BL Lacs no evolution within one σ is apparent.

12. The gamma-ray luminosity function of bright FSRQs can be described by a single power-law with index ~ 2.5 and ~ 1.5 for the high (≥ 0.9) and low (≤ 0.9) redshift range, respectively, while the BL Lac gamma-ray luminosity function follows a power law with index ~ 2.1. The space density of gamma-ray emitting BL Lacs of ~ 190 Gpc^{-3} above their limiting luminosity, $\sim 3 \times 10^{44}$erg s^{-1}, is a factor ~ 200 larger than for the *Fermi*-detected FSRQ population above their limiting luminosity, $\sim 7 \times 10^{45}$erg s^{-1}. Thus, within the *Fermi* bright AGN list BL Lacs are intrinsically more numerous than FSRQs. Bright Fermi detected BL Lacs and FSRQs display comparable cumulative number counts above $\sim 10^{47}$erg s^{-1}, with BL Lacs being ~ 3 times more numerous than FSRQs.

These early results from the first three months of the science mission of the *Fermi Gamma ray Space Telescope* demonstrate its exceptional capabilities to provide important new knowledge about γ-ray emission from active galactic nuclei and blazars. As the *Fermi*-LAT data accumulate, many more AGNs at lower flux levels will likely be detected- as well as flaring AGNs at brighter fluxes than yet observed - helping to refine these results and improve our understanding of supermassive black holes.

10. Acknowledgments

The *Fermi* LAT Collaboration acknowledges the generous support of a number of agencies and institutes that have supported the *Fermi* LAT Collaboration. These include the National Aeronautics and Space Administration and the Department of Energy in the United States, the Commissariat à l'Energie Atomique and the Centre National de la Recherche Scientifique / Institut

National de Physique Nucléaire et de Physique des Particules in France, the Agenzia Spaziale Italiana and the Istituto Nazionale di Fisica Nucleare in Italy, the Ministry of Education, Culture, Sports, Science and Technology (MEXT), High Energy Accelerator Research Organization (KEK) and Japan Aerospace Exploration Agency (JAXA) in Japan, and the K. A. Wallenberg Foundation, the Swedish Research Council and the Swedish National Space Board in Sweden.

Additional support for science analysis during the operations phase from the following agencies is also gratefully acknowledged: the Istituto Nazionale di Astrofisica in Italy and the K. A. Wallenberg Foundation in Sweden for providing a grant in support of a Royal Swedish Academy of Sciences Research fellowship for JC.

MA acknowledges N. Cappelluti for extensive discussion about the sky coverage.

Facilities: *Fermi* LAT.

REFERENCES

Abdo, A. A., et al. 2009a, ApJ, submitted - LAT 3C454.3

—. 2009b, ApJ, in preparation - LAT NGC 1275

—. 2009c, ApJ, submitted - LAT Bright Source List

Aharonian, F., et al. 2009, ApJ, submitted

Ajello, M., et al. 2009, ApJ, submitted

—. 2008, ApJ, 673, 96

Atwood, W. B., et al. 2009, ApJ, submitted, arXiv:astro-ph/0902.1089

Avni, Y. 1976, ApJ, 210, 642

Avni, Y., & Bahcall, J. N. 1980, ApJ, 235, 694

Beckmann, V., Engels, D., Bade, N., & Wucknitz, O. 2003, A&A, 401, 927

Bhattacharya, D., Sreekumar, P., & Mukherjee, R. 2008, ArXiv e-prints

Blandford, R. D., & Rees, M. J. 1978, in BL Lac Objects, ed. A. M. Wolfe, 328–341

Böttcher, M. 2007, Ap&SS, 309, 95

Böttcher, M., & Dermer, C. D. 2002, ApJ, 564, 86

Cappelluti, N., et al. 2007, ApJS, 172, 341

Casandjian, J.-M., & Grenier, I. A. 2008, A&A, 489, 849

Cavaliere, A., & D'Elia, V. 2002, ApJ, 571, 226

Ciprini, S., et al. 2007, in American Institute of Physics Conference Series, Vol. 921, The First GLAST Symposium, ed. S. Ritz, P. Michelson, & C. A. Meegan, 546–547

Condon, J. J., Cotton, W. D., Greisen, E. W., Yin, Q. F., Perley, R. A., Taylor, G. B., & Broderick, J. J. 1998, AJ, 115, 1693

de Ruiter, H. R., Arp, H. C., & Willis, A. G. 1977, A&AS, 28, 211

della Ceca, R., Lamorani, G., Maccacaro, T., Wolter, A., Griffiths, R., Stocke, J. T., & Setti, G. 1994, ApJ, 430, 533

Dermer, C. D. 2007, ApJ, 659, 958

Dermer, C. D., Razzaque, S., Finke, J. D., & Atoyan, A. 2008, ArXiv e-prints

Fichtel, C. E., et al. 1994, ApJS, 94, 551

Foschini, L., et al. 2005, A&A, 433, 515

Fossati, G., Maraschi, L., Celotti, A., Comastri, A., & Ghisellini, G. 1998, MNRAS, 299, 433

Ghisellini, G., Celotti, A., Fossati, G., Maraschi, L., & Comastri, A. 1998, MNRAS, 301, 451

Giommi, P., Colafrancesco, S., Cavazzuti, E., Perri, M., & Pittori, C. 2006, A&A, 445, 843

Giovannini, G., Feretti, L., Gregorini, L., & Parma, P. 1988, A&A, 199, 73

Gregory, P. C., Scott, W. K., Douglas, K., & Condon, J. J. 1996, ApJS, 103, 427

Griffith, M. R., & Wright, A. E. 1993, AJ, 105, 1666

Hartman, R. C., et al. 1999, ApJS, 123, 79

Hasinger, G., Burg, R., Giacconi, R., Hartner, G., Schmidt, M., Trumper, J., & Zamorani, G. 1993, A&A, 275, 1

Hasinger, G., Miyaji, T., & Schmidt, M. 2005, A&A, 441, 417

Healey, S. E., et al. 2008, ApJS, 175, 97

Healey, S. E., Romani, R. W., Taylor, G. B., Sadler, E. M., Ricci, R., Murphy, T., Ulvestad, J. S., & Winn, J. N. 2007, ApJS, 171, 61

Hogg, D. W. 1999, ArXiv Astrophysics e-prints

Inoue, Y., & Totani, T. 2008, ArXiv e-prints, submitted

Ivezić, Ž., et al. 2002, AJ, 124, 2364

Jorstad, S. G., Marscher, A. P., Mattox, J. R., Wehrle, A. E., Bloom, S. D., & Yurchenko, A. V. 2001, ApJS, 134, 181

Kellermann, K. I., et al. 2004, ApJ, 609, 539

Komatsu, E., et al. 2008, ArXiv e-prints

Maraschi, L., Ghisellini, G., & Celotti, A. 1992, ApJ, 397, L5

Massaro, E., Giommi, P., Sclavi, S., Perri, M., Piranomonte, S., Leto, C., & Maselli, A. 2007, in American Institute of Physics Conference Series, Vol. 921, The First GLAST Symposium, ed. S. Ritz, P. Michelson, & C. A. Meegan, 349–350

Mattox, J. R., Hartman, R. C., & Reimer, O. 2001, ApJS, 135, 155

Mauch, T., Murphy, T., Buttery, H. J., Curran, J., Hunstead, R. W., Piestrzynski, B., Robertson, J. G., & Sadler, E. M. 2003, MNRAS, 342, 1117

Mücke, A., & Pohl, M. 2000, MNRAS, 312, 177

Mücke, A., et al. 1997, A&A, 320, 33

Mukherjee, R., et al. 1997, ApJ, 490, 116

Mukherjee, R., Halpern, J., Mirabal, N., & Gotthelf, E. V. 2002, ApJ, 574, 693

Nandikotkur, G., Jahoda, K. M., Hartman, R. C., Mukherjee, R., Sreekumar, P., Böttcher, M., Sambruna, R. M., & Swank, J. H. 2007, ApJ, 657, 706

Narumoto, T., & Totani, T. 2006, ApJ, 643, 81

Padovani, P., Giommi, P., Landt, H., & Perlman, E. S. 2007, ApJ, 662, 182

Pittori, C., et al. 2008, A&A, submitted - AGILE Catalog

Pohl, M., Hartman, R. C., Jones, B. B., & Sreekumar, P. 1997, A&A, 326, 51

Rector, T. A., Stocke, J. T., Perlman, E. S., Morris, S. L., & Gioia, I. M. 2000, AJ, 120, 1626

Schmidt, M. 1968, ApJ, 151, 393

Silverman, J. D., et al. 2008, ApJ, 679, 118

Sowards-Emmerd, D., Romani, R. W., & Michelson, P. F. 2003, ApJ, 590, 109

Sreekumar, P., et al. 1998, ApJ, 494, 523

Sreekumar, P., Bertsch, D. L., Hartman, R. C., Nolan, P. L., & Thompson, D. J. 1999, Astroparticle Physics, 11, 221

Starck, J.-L., & Pierre, M. 1998, A&AS, 128, 397

Stecker, F. W., & Salamon, M. H. 1996, ApJ, 464, 600

Stecker, F. W., & Salamon, M. H. 2001, in American Institute of Physics Conference Series, Vol. 587, Gamma 2001: Gamma-Ray Astrophysics, ed. S. Ritz, N. Gehrels, & C. R. Shrader, 432–+

Sutherland, W., & Saunders, W. 1992, MNRAS, 259, 413

Tavani, M., et al. 2008, Nuclear Instruments and Methods in Physics Research A, 588, 52

The Pierre AUGER Collaboration, et al. 2007, Science, 318, 938

Thompson, D. J., et al. 1995, ApJS, 101, 259

—. 1993, ApJS, 86, 629

Ueda, Y., Akiyama, M., Ohta, K., & Miyaji, T. 2003, ApJ, 598, 886

Urry, C. M., & Padovani, P. 1995, PASP, 107, 803

Venters, T. M., & Pavlidou, V. 2007, ApJ, 666, 128

Voges, W., et al. 1999, A&A, 349, 389

Wall, J. V., Jackson, C. A., Shaver, P. A., Hook, I. M., & Kellermann, K. I. 2005, A&A, 434, 133

Waxman, E., & Bahcall, J. 1999, Phys. Rev. D, 59, 023002

This preprint was prepared with the AAS LaTeX macros v5.2.

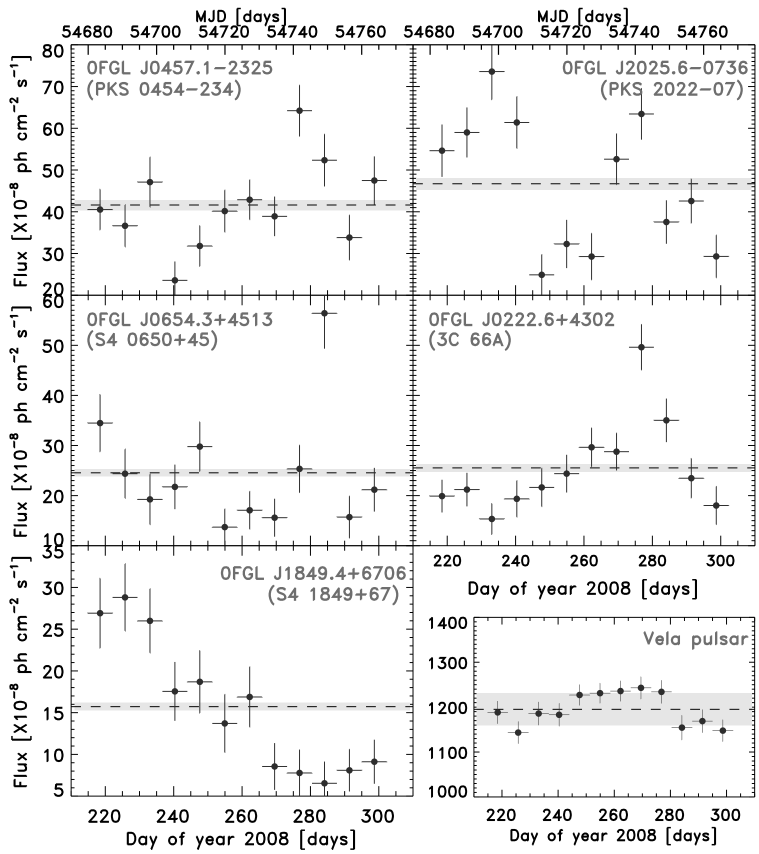

Fig. 1.— Examples of weekly light curves for five bright blazars detected by *Fermi*-LAT and the Vela light curve for comparison (flux unit: $\times 10^{-8}$ photons cm^{-2} s-1, please note the different scales). The dashed line is the average value and the grey area shows the 3% systematic error we have adopted. Different flux variability amplitudes and timescales are clearly visible in the blazar light curves.

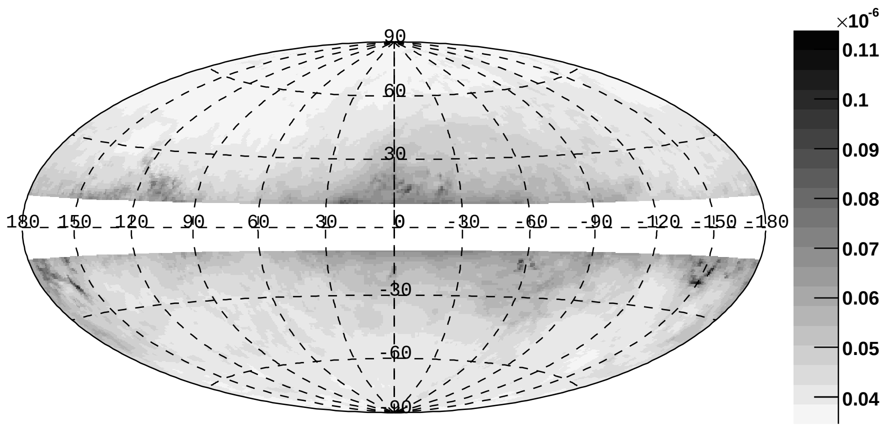

Fig. 2.— Flux limit [E>100 MeV] (ph $cm^{-2}s^{-1}$) as a function of sky location (in galactic coordinates), for a photon index=2.2

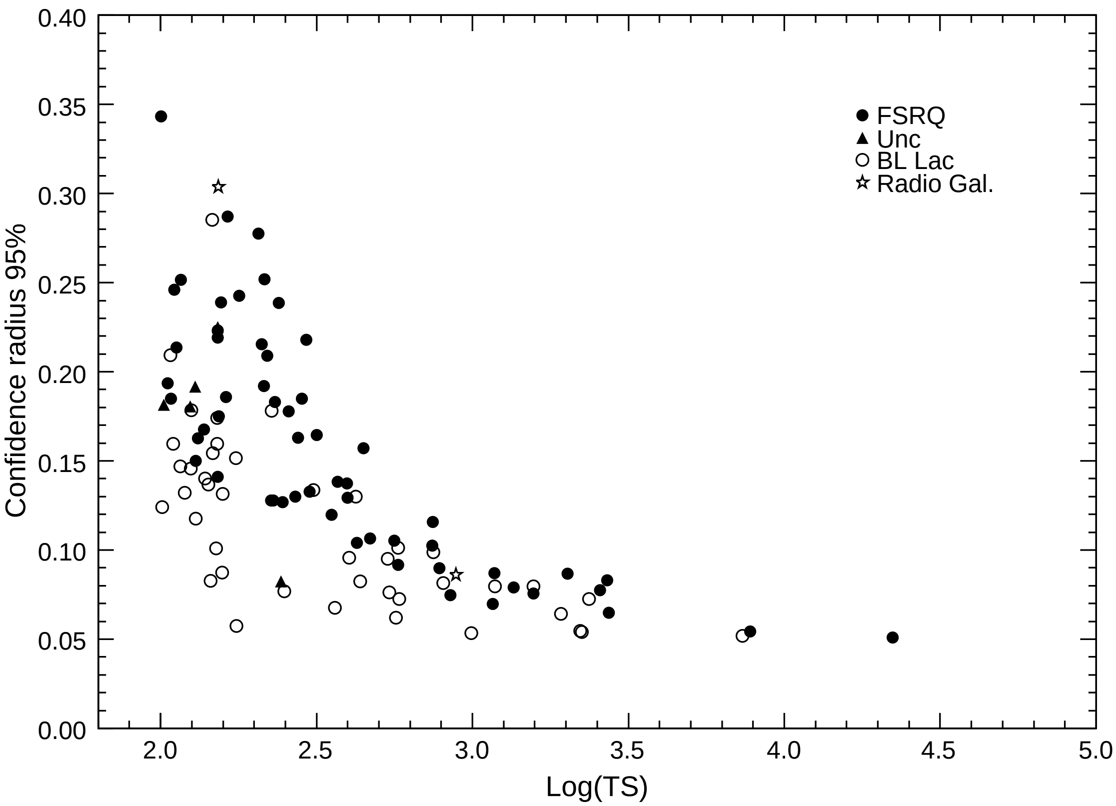

Fig. 3.— 95% error radius as a function of TS for the sources presented in this paper. FSRQs: closed circles, BL Lacs: open circles, Uncertain type: closed triangles, Radio galaxies: open stars.

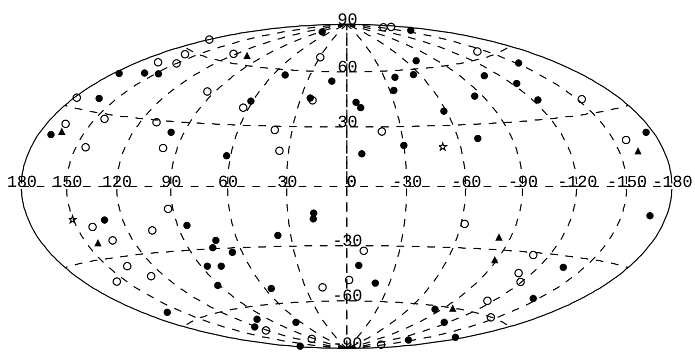

Fig. 4.— Location of the LBAS sources. FSRQs: closed circles, BL Lacs: open circles, Uncertain type: closed triangles, RG: open stars.

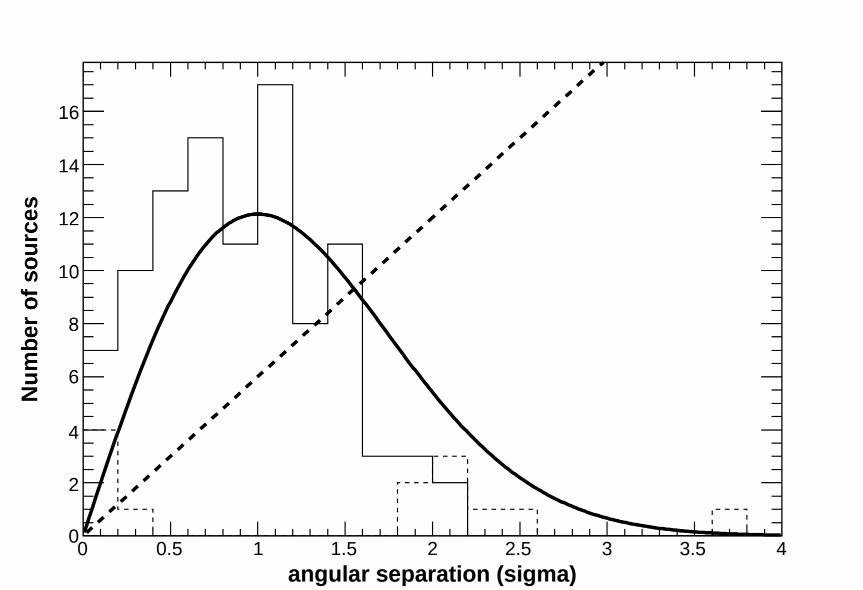

Fig. 5.— Normalized angular separation between the *Fermi*-LAT location and that of the counterpart. The solid (dashed) histogram corresponds to the sources with high-(low-) confidence associations. The solid curve corresponds to the expected distribution (χ^2 distribution with 2 d.o.f.) for real associations, the dashed one for accidental associations.

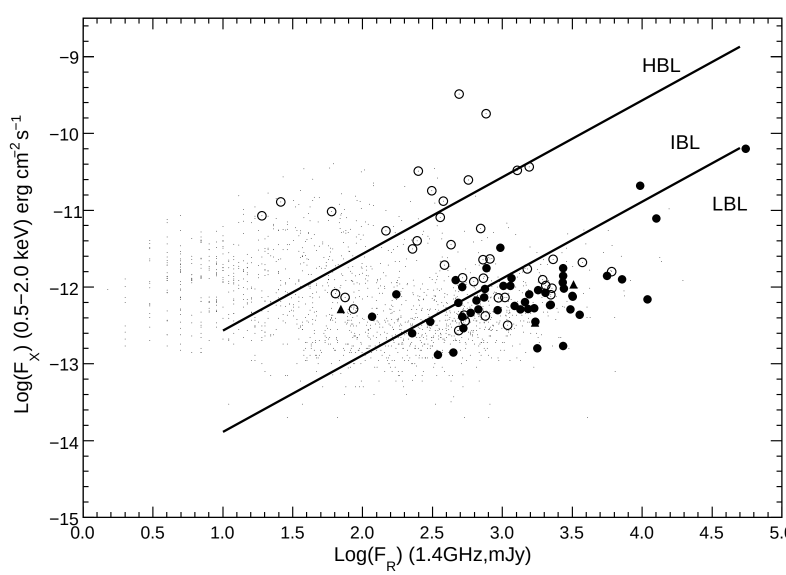

Fig. 6.— The X-ray (0.5 - 2.0 keV) vs radio flux density (1.4 GHz) plot of all X-ray detected blazars in the BZCAT catalog (small dots) and the *Fermi*-LAT detected blazars (BL Lacs: open circles, FSRQs: filled circles, blazars of uncertain type: triangles, radio galaxies: stars).

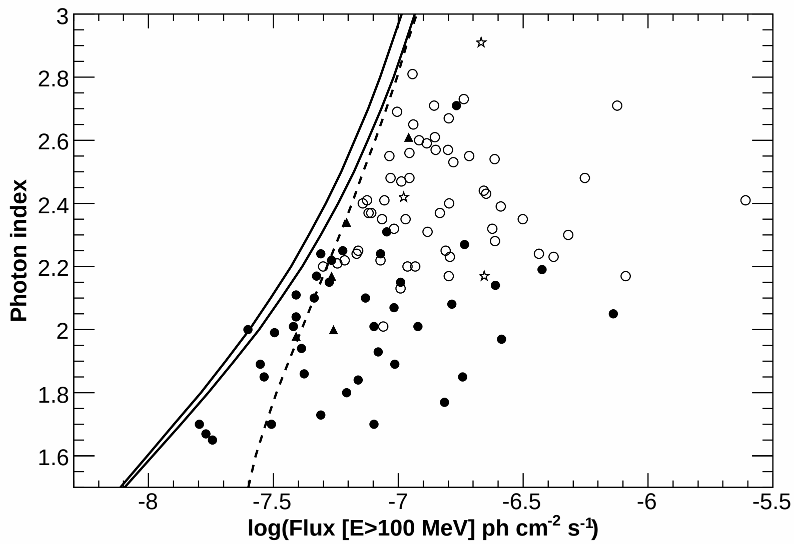

Fig. 7.— Flux [E>100 MeV] vs photon index for the 116 sources. FSRQs: closed circles, BL Lacs: open circles, Uncertain type: closed triangles, Radio galaxies: open stars. The solid curves represent the TS=100 limit estimated for two galactic latitudes b=20° and b=80° . The dashed curve represents the TS=100 limit for b=80° and 0.2 <E< 3 GeV.

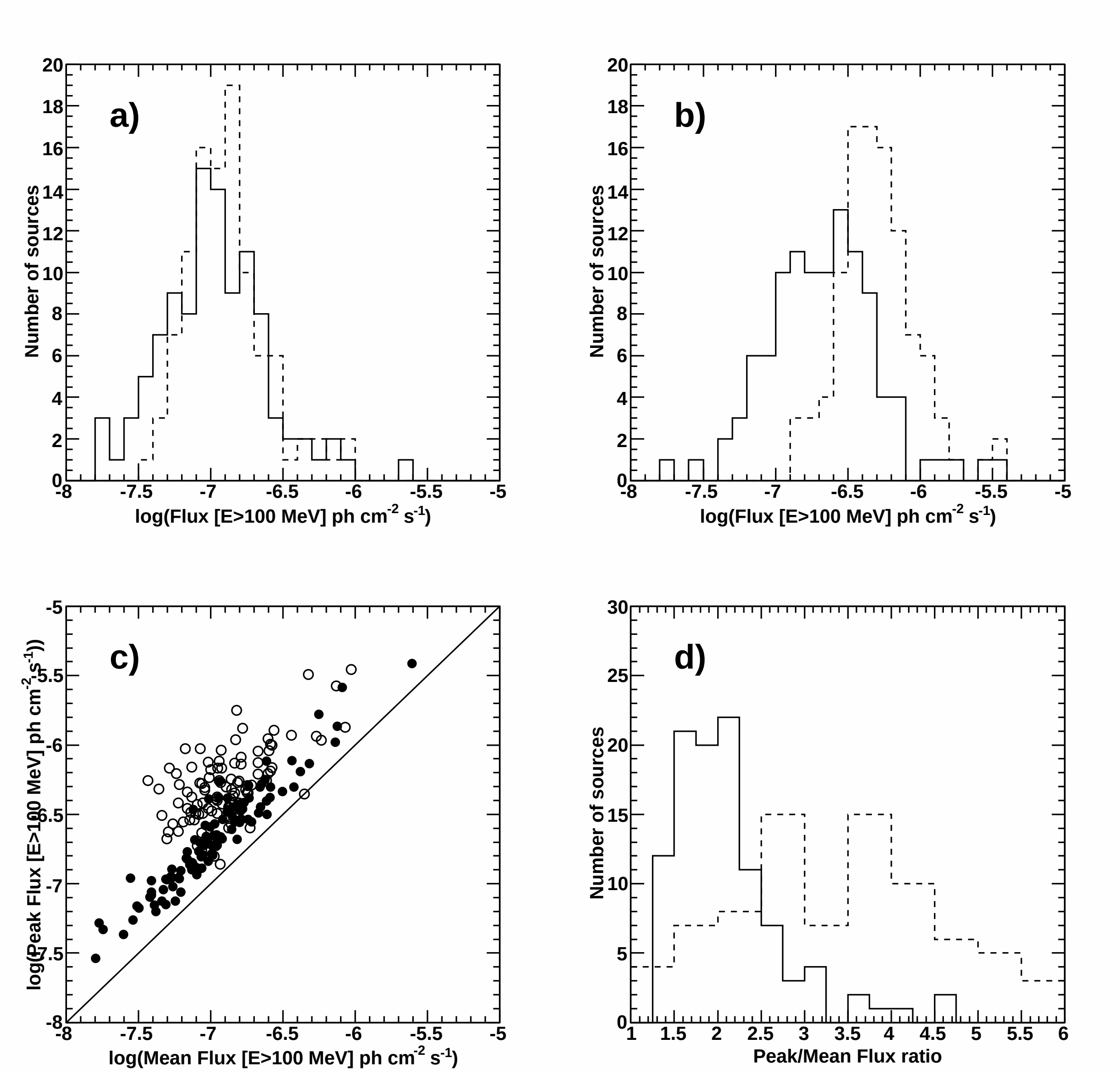

Fig. 8.— a) Comparison of mean flux distribution for blazars detected by *Fermi*-LAT (solid) and *EGRET* (dashed). b) same of as a), for the peak flux distribution. c) Peak flux as a function of mean flux, for the *Fermi*-LAT (closed circles) and *EGRET* (open circles) AGNs. d) same as a), for the peak/mean flux ratio.

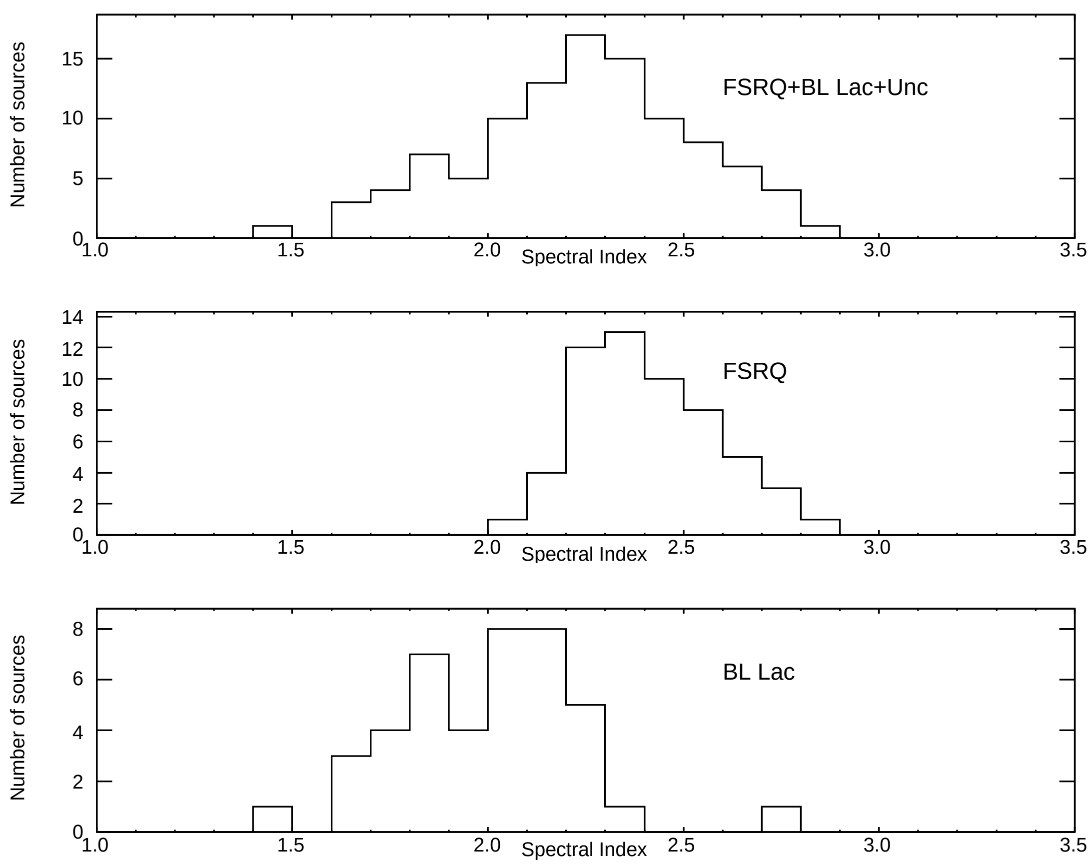

Fig. 9.— Photon index distributions for the LBAS blazars. Top: All sources. Middle: FSRQs. Bottom: BL Lacs.

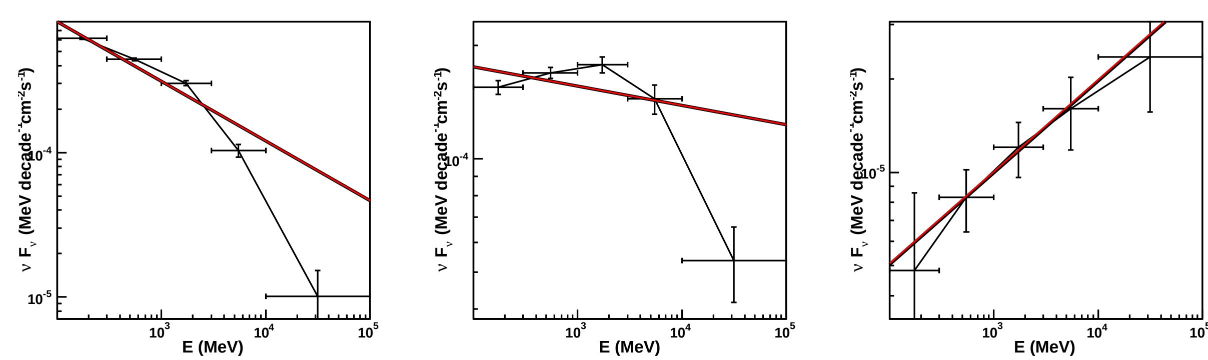

Fig. 10.— Gamma-ray SED of 3 bright blazars calculated in five energy bands, compared with the power law fitted over the whole energy range. Left: 3C454.3 (FSRQ), middle: AO 0235+164 (IBL), right: Mkn 501 (HBL)

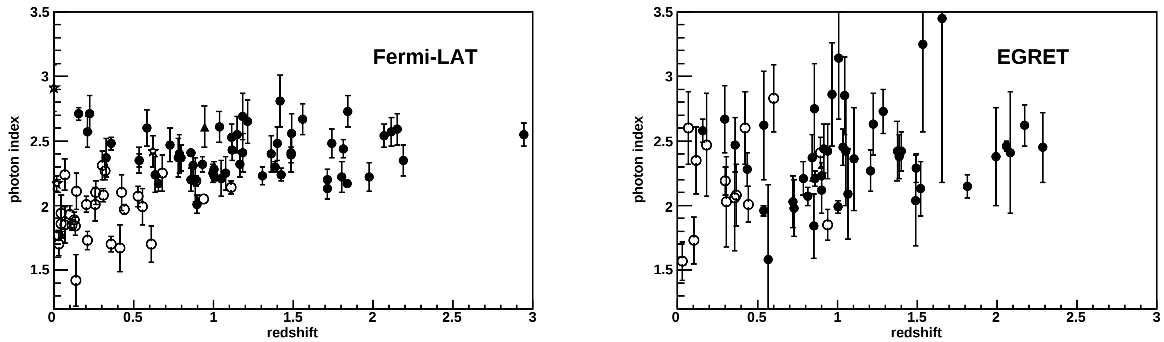

Fig. 11.— Left: LBAS photon index as a function of redshift. Same symbols as before. Right: same as left, for the *EGRET* sample.

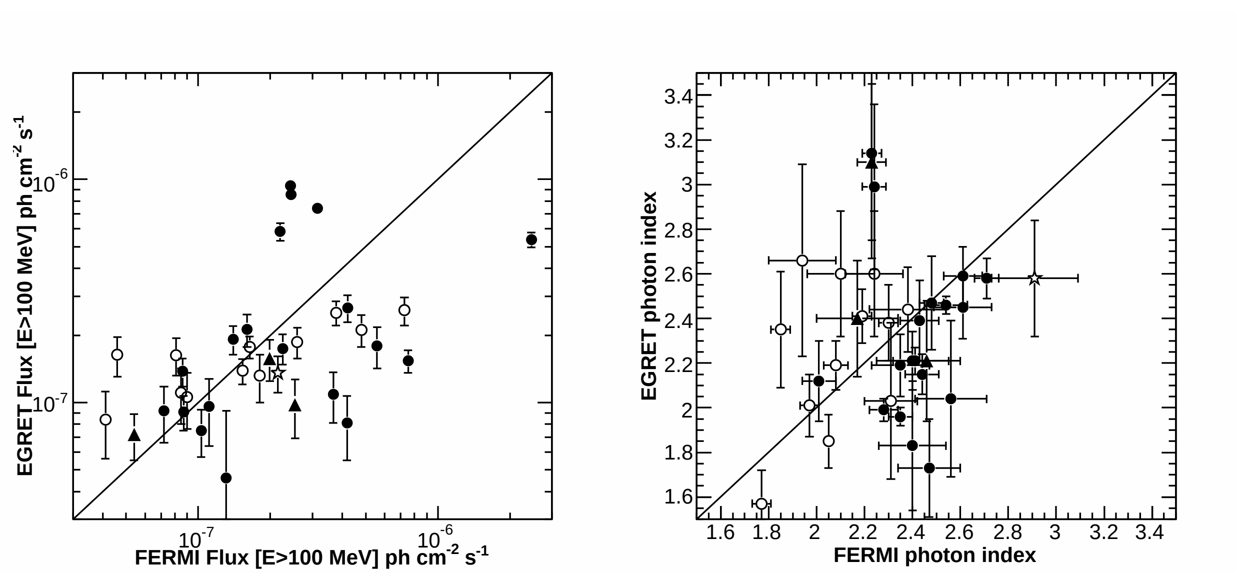

Fig. 12.— Left: *Fermi*-LAT vs *EGRET* mean flux for the 33 AGNs present in both samples FSRQs: closed circles, BL Lacs: open circles, Uncertain type: closed triangles. Right: same as left, for photon index.

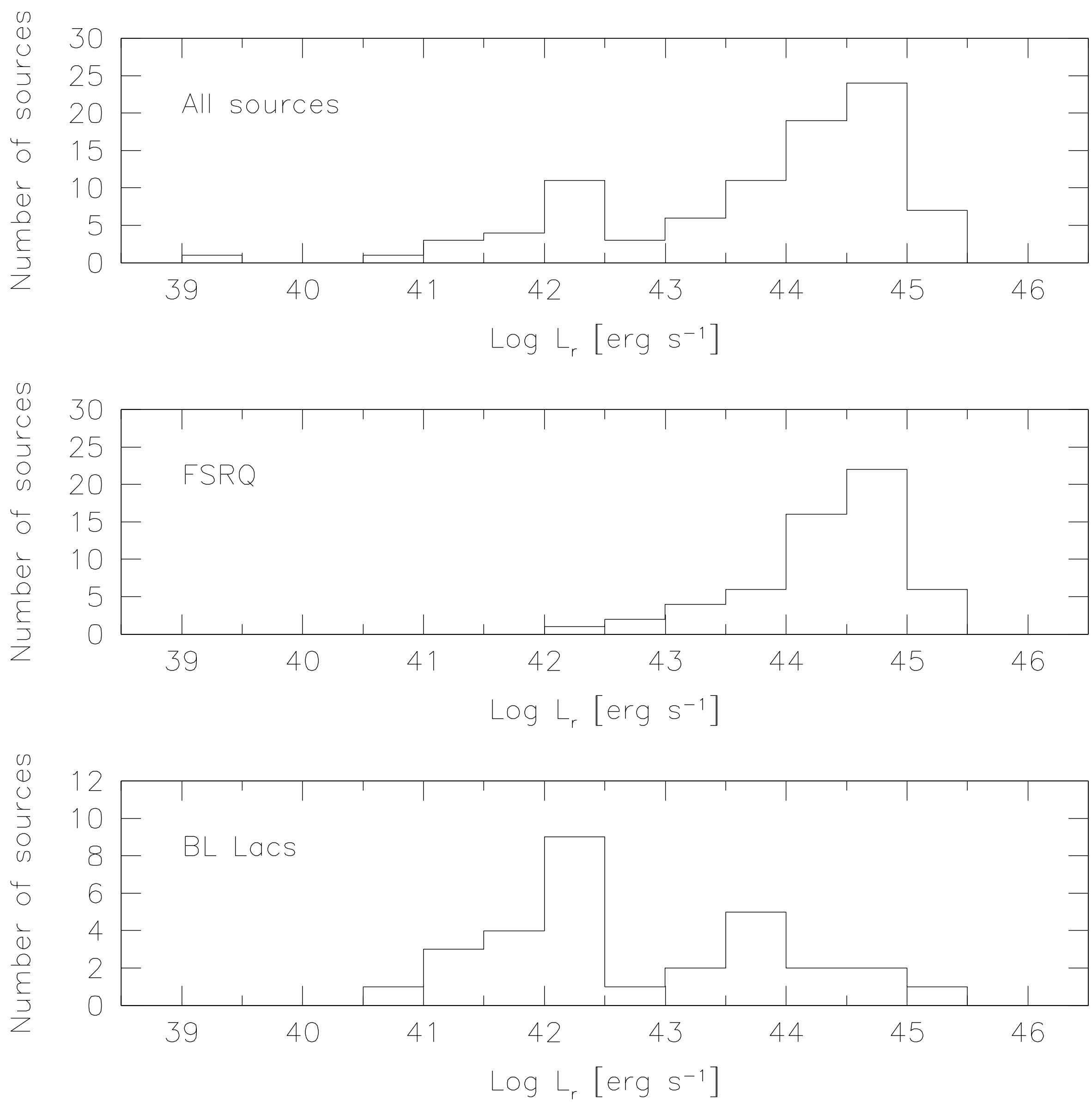

Fig. 13.— Histogram of the radio power distribution for LBAS sources, for all sources (upper panel), FSRQs (middle), and BL Lacs (bottom) only.

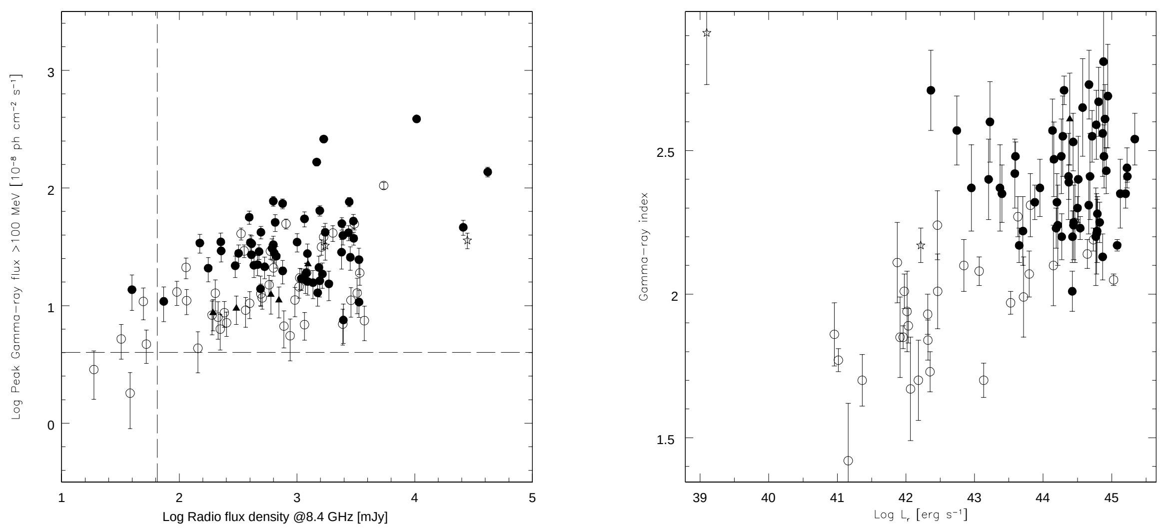

Fig. 14.— Radio vs. gamma-ray properties. Left: peak gamma-ray flux vs. radio flux density at 8.4 GHz; the dashed lines show the CRATES flux density limit and the typical LAT detection threshold. Right: gamma-ray photon index vs. radio luminosity.

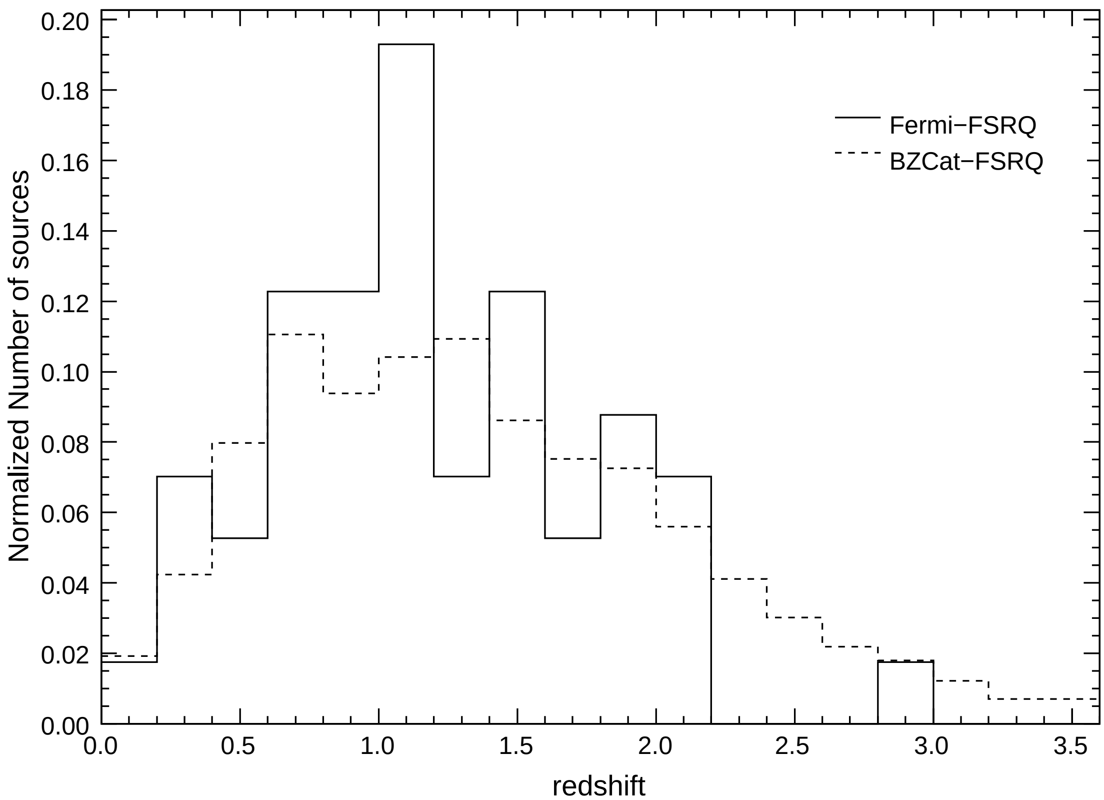

Fig. 15.— Redshift distribution for the FSRQs in the LBAS (solid) and in the BZCat catalog (dashed).

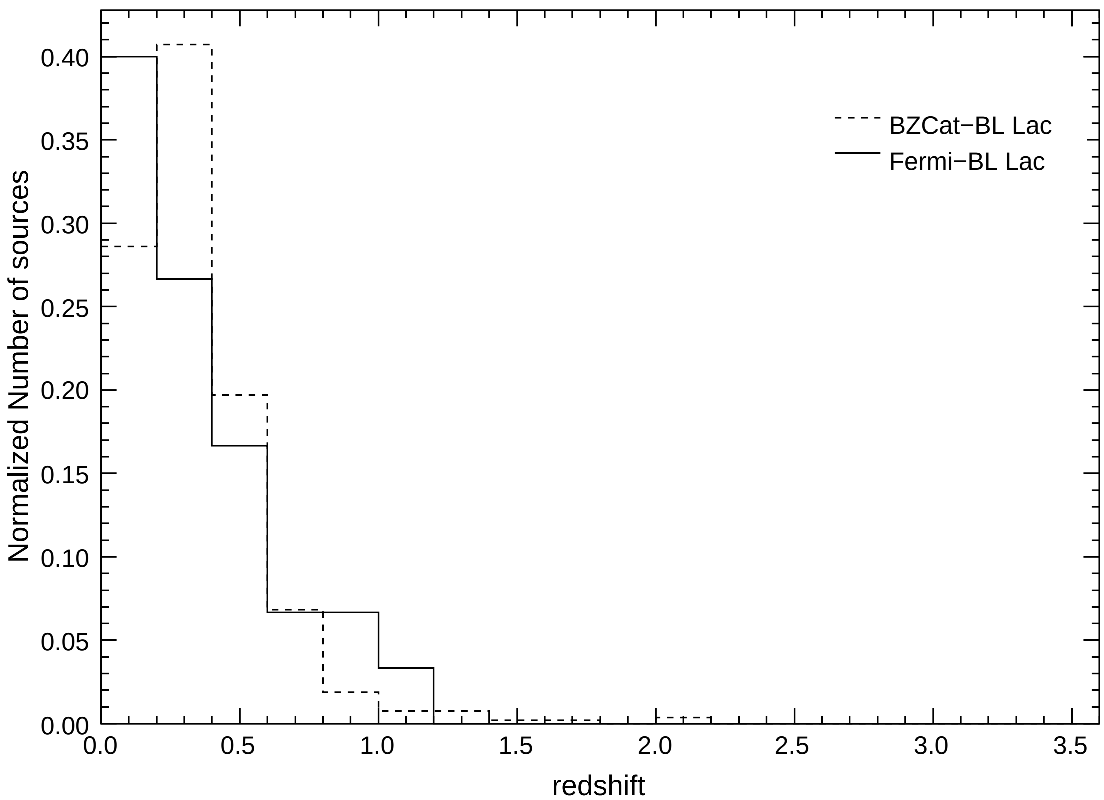

Fig. 16.— Redshift distribution for the BL Lacs in the LBAS (solid) and in the BZCat catalog (dashed).

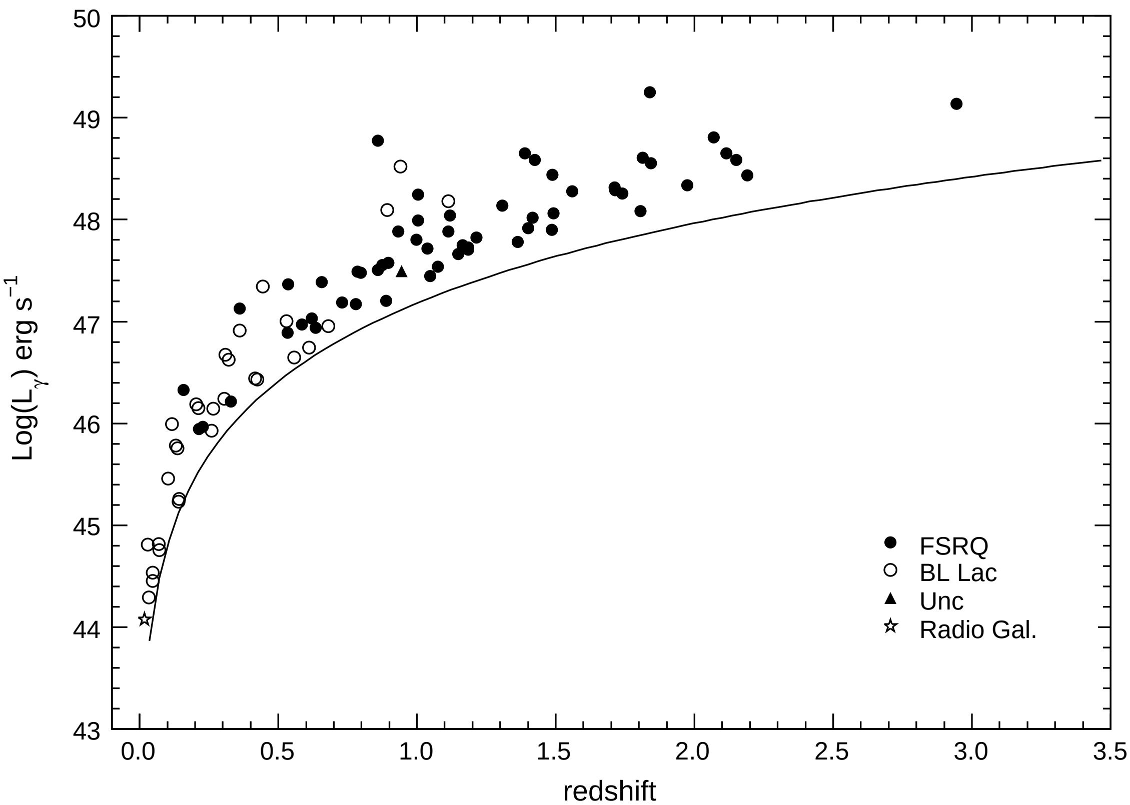

Fig. 17.— Gamma-ray Luminosity vs redshift for the LBAS. The solid line was drawn using a $F_{100} = 4 \times 10^{-8}$ ph cm^{-2} s^{-1}and a photon index of 2.2.

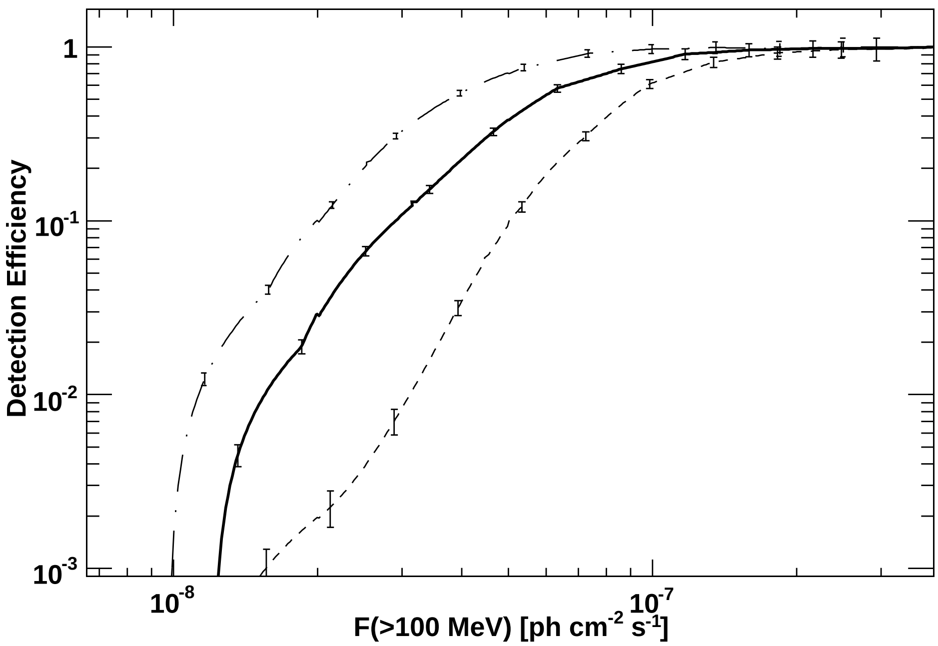

Fig. 18.— Detection efficiencies in the LAT |b| ≥10° survey as a function of flux. The solid line is for the entire blazar population while the dashed and long-dashed are for the FSRQs and BL Lacs respectively. The errors on the detection efficiency are due to the counting statistics in our Monte Carlo simulations.

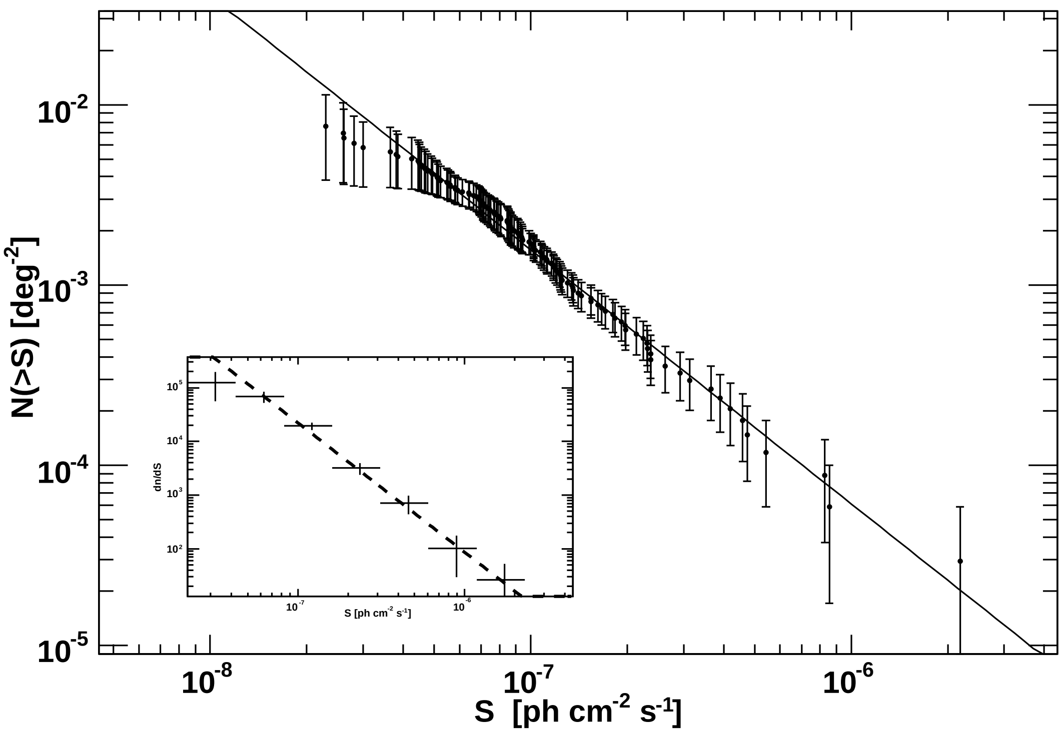

Fig. 19.— Source count distribution for the whole extragalactic population (excluding the pulsars). The dashed line is the best power-law fit to the F(>100 MeV)$\geq 7 \times 10^{-8}$ ph cm^{-2} s^{-1} data. The inset shows the differential distribution.

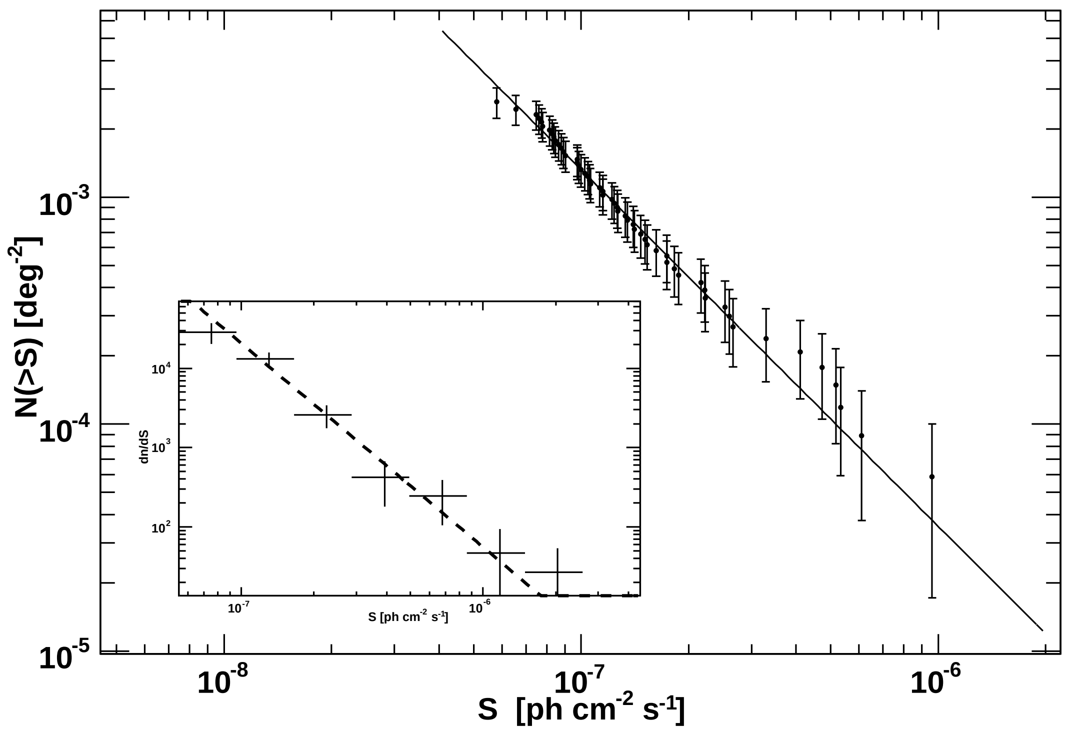

Fig. 20.— Source count distribution for FSRQs. The dashed line is the best power-law fit to the F(>100 MeV)$\geq 7 \times 10^{-8}$ ph cm^{-2} s^{-1} data. The inset shows the differential distribution.

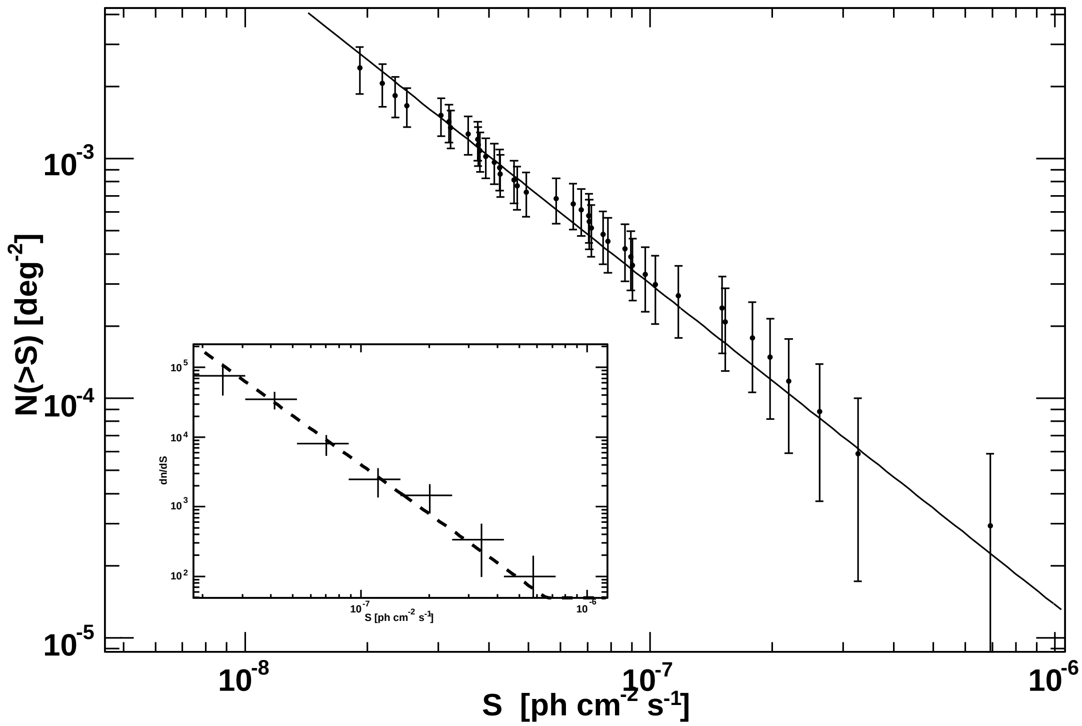

Fig. 21.— Source count distribution for BL Lacs. The dashed line is the best power-law fit to the F(>100 MeV)$\geq 3 \times 10^{-8}$ ph cm^{-2} s^{-1} data. The inset shows the differential distribution.

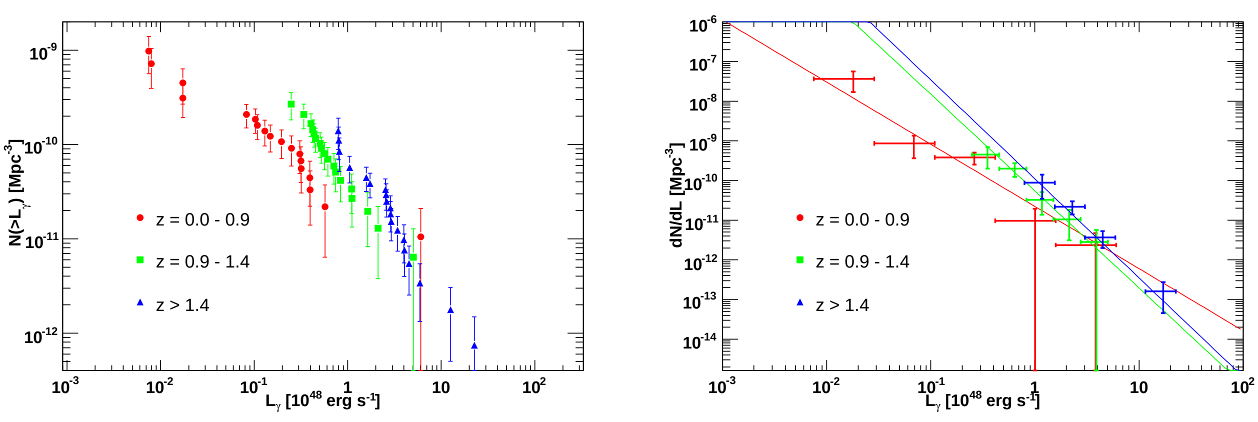

Fig. 22.— Luminosity functions of FSRQs in bins of redshift. The cumulative and differential distributions are shown, respectively, on the left and on the right panel. The (color-coded) solid lines are the ML fits to the 3 different datasets using a simple power law to model the GLF.

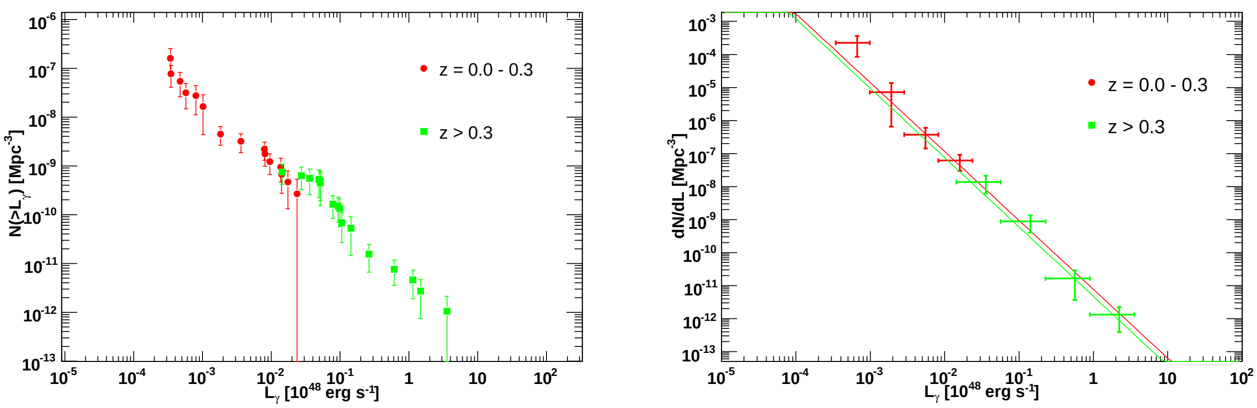

Fig. 23.— Luminosity functions of BL Lacs in bins of redshift. The cumulative and differential distributions are shown, respectively, on the left and on the right panel. The (color-coded) solid lines are the ML fits to the 2 different datasets using a simple power law to model the GLF.

Table 1. The high-confidence association Bright AGN List

	FoM			*gtsrcid*				
LAT Name	Source Name	FoM	Prob.	Source Name	Prob.	Other Names	z	Class
0FGL J0017.4−0503	CGRaBS J0017−0512	16.20	0.93	CGRaBS J0017−0512	0.92	· · ·	0.227	FSRQ
0FGL J0033.6−1921	· · ·	· · ·	· · ·	BZB J0033−1921	0.99	KUV 00311−1938	0.610	BLLac
0FGL J0050.5−0928	CGRaBS J0050−0929	61.01	1.00	CRATES J0050−0929	0.99	PKS 0048−097	· · ·	BLLac
0FGL J0051.1−0647	CGRaBS J0051−0650	42.95	0.98	CRATES J0051−0650	0.99	PKS 0048−071	1.975	FSRQ
0FGL J0112.1+2247	CGRaBS J0112+2244	48.96	0.98	S2 0109+22	1.00	S2 0109+22	0.265	BLLac
0FGL J0118.7−2139	CGRaBS J0118−2141	35.02	0.97	CGRaBS J0118−2141	0.99	PKS 0116−219	1.165	FSRQ
0FGL J0120.5−2703	CGRaBS J0120−2701	60.25	1.00	PKS 0118−272	1.00	PKS 0118−272	0.557	BLLac
0FGL J0136.6+3903	BZB J0136+3905	12.45	0.91	B3 0133+388	1.00	B3 0133+388	· · ·	BLLac
0FGL J0137.1+4751	CGRaBS J0136+4751	52.21	0.99	CGRaBS J0136+4751	0.99	DA 55	0.859	FSRQ
0FGL J0144.5+2709	CRATES J0144+2705	30.93	0.96	CRATES J0144+2705	0.58	TXS 0141+268	· · ·	BLLac
0FGL J0145.1−2728	CGRaBS J0145−2733	37.41	0.97	CGRaBS J0145−2733	0.96	PKS 0142−278	1.148	FSRQ
0FGL J0204.8−1704	CGRaBS J0204−1701	55.22	0.99	CGRaBS J0204−1701	0.96	PKS 0202−17	1.740	FSRQ
0FGL J0210.8−5100	CGRaBS J0210−5101	69.87	1.00	PKS 0208−512	1.00	PKS 0208−512	1.003	FSRQ
0FGL J0217.8+0146	CGRaBS J0217+0144	52.67	0.99	CGRaBS J0217+0144	1.00	PKS 0215+015	1.715	FSRQ
0FGL J0220.9+3607	CGRaBS J0221+3556	7.66	0.89	CGRaBS J0221+3556	0.95	B2 0218+35	0.944	Unc***
0FGL J0222.6+4302	BZB J0222+4302	23.18	0.95	3C 66A	1.00	3C 66A	0.444	BLLac
0FGL J0229.5−3640	BZQ J0229−3643	29.20	0.96	BZQJ0229−3643	0.94	PKS 0227−369	2.115	FSRQ
0FGL J0238.6+1636	CGRaBS J0238+1636	60.54	1.00	CGRaBS J0238+1636	1.00	AO 0235+164	0.940	BLLac
0FGL J0245.6−4656	CRATES J0246−4651	23.23	0.95	CRATES J0246−4651	0.54	PKS 0244−470	· · ·	Unc***
0FGL J0303.7−2410	CRATES J0303−2407	9.32	0.90	PKS 0301−243	1.00	PKS 0301−243	0.260	BLLac
0FGL J0320.0+4131	CGRaBS J0319+4130	33.67	0.97	0316+413	1.00	NGC 1275	0.018	RG
0FGL J0334.1−4006	CGRaBS J0334−4008	63.24	1.00	PKS 0332−403	1.00	PKS 0332−403	· · ·	BLLac
0FGL J0349.8−2102	CGRaBS J0349−2102	47.40	0.98	CGRaBS J0349−2102	0.99	PKS 0347−211	2.944	FSRQ
0FGL J0428.7−3755	CGRaBS J0428−3756	54.09	0.99	CGRaBS J0428−3756	1.00	PKS 0426−380	1.112	BLLac
0FGL J0449.7−4348	CRATES J0449−4350	5.52	0.81	PKS 0447−439	1.00	PKS 0447−439	0.205	BLLac
0FGL J0457.1−2325	CGRaBS J0457−2324	35.74	0.97	CGRaBS J0457−2324	1.00	PKS 0454−234	1.003	FSRQ
0FGL J0507.9+6739	BZB J0507+6737	4.74	0.76	1ES 0502+675	1.00	1ES 0502+675	0.416	BLLac
0FGL J0516.2−6200	CGRaBS J0516−6207	12.04	0.91	CGRaBS J0516−6207	0.94	PKS 0516−621	· · ·	Unc***
0FGL J0531.0+1331	CGRaBS J0530+1331	65.48	1.00	CRATES J0530+1331	1.00	PKS 0528+134	2.070	FSRQ
0FGL J0538.8−4403	CRATES J0538−4405	53.80	0.99	BZBJ0538−4405	0.99	PKS 0537−441	0.892	BLLac
0FGL J0654.3+4513	CGRaBS J0654+4514	42.13	0.98	CGRaBS J0654+4514	1.00	B3 0650+453	0.933	FSRQ
0FGL J0654.3+5042	CGRaBS J0654+5042	49.98	0.99	CGRaBS J0654+5042	1.00	· · ·	· · ·	Unc***
0FGL J0700.0−6611	CRATES J0700−6610	33.82	0.97	CRATES J0700−6610	0.64	PKS 0700−661	· · ·	Unc***
0FGL J0712.9+5034	CGRaBS J0712+5033	44.20	0.98	CGRaBS J0712+5033	0.99	· · ·	· · ·	BLLac
0FGL J0714.2+1934	CLASS J0713+1935	20.54	0.94	· · ·	· · ·	· · ·	0.534	FSRQ
0FGL J0719.4+3302	CRATES J0719+3307	14.33	0.92	BZUJ0719+3307	0.89	TXS 0716+332	0.779	FSRQ
0FGL J0722.0+7120	CGRaBS J0721+7120	66.40	1.00	CRATES J0721+7120	1.00	S5 0716+71	0.310	BLLac
0FGL J0738.2+1738	CGRaBS J0738+1742	25.45	0.95	PKS 0735+17	1.00	PKS 0735+178	0.424	BLLac
0FGL J0818.3+4222	CGRaBS J0818+4222	61.26	1.00	OJ 425	1.00	OJ 425	0.530	BLLac
0FGL J0824.9+5551	CGRaBS J0824+5552	57.80	0.99	CGRaBS J0824+5552	0.98	TXS 0820+560	1.417	FSRQ
0FGL J0855.4+2009	CGRaBS J0854+2006	8.67	0.90	OJ 287	0.99	OJ 287	0.306	BLLac
0FGL J0921.2+4437	CGRaBS J0920+4441	13.49	0.92	CGRaBS J0920+4441	0.95	RGB J0920+446	2.190	FSRQ
0FGL J0948.3+0019	CGRaBS J0948+0022	18.64	0.93	CGRaBS J0948+0022	0.94	PMN J0948+0022	0.585	FSRQ
0FGL J0957.6+5522	CRATES J0957+5522	50.91	0.99	BZQJ0957+5522	0.96	4C +55.17	0.896	FSRQ
0FGL J1012.9+2435	CRATES J1012+2439	13.63	0.92	· · ·	· · ·	· · ·	1.805	FSRQ
0FGL J1015.2+4927	CGRaBS J1015+4926	18.06	0.93	1ES 1011+496	1.00	1ES 1011+496	0.212	BLLac
0FGL J1015.9+0515	CRATES J1016+0513	28.86	0.96	CRATES J1016+0513	0.78	PMN J1016+0512	1.713	FSRQ
0FGL J1034.0+6051	CGRaBS J1033+6051	52.57	0.99	CGRaBS J1033+6051	0.98	S4 1030+61	1.401	FSRQ
0FGL J1053.7+4926	BZB J1053+4929	11.55	0.91	MS 1050.7+4946	1.00	MS 1050.7+4946	0.140	BLLac
0FGL J1054.5+2212	CLASS J1054+2210	16.20	0.93	· · ·	· · ·	· · ·	· · ·	BLLac
0FGL J1057.8+0138	CGRaBS J1058+0133	3.71	0.68	CGRaBS J1058+0133	0.93	PKS 1055+018	0.888	FSRQ
0FGL J1058.9+5629	CGRaBS J1058+5628	24.66	0.95	RXS J10586+5628	1.00	RXS J10586+5628	0.143	BLLac
0FGL J1100.2−8000	CGRaBS J1058−8003	53.65	0.99	CGRaBS J1058−8003	0.99	PKS 1057−79	· · ·	BLLac
0FGL J1104.5+3811	CGRaBS J1104+3812	35.10	0.97	Mrk 421	1.00	Mrk 421	0.030	BLLac
0FGL J1129.8−1443	CRATES J1130−1449	27.54	0.96	BZQ J1130−1449	0.84	PKS 1127−14	1.184	FSRQ
0FGL J1146.7−3808	CGRaBS J1147−3812	45.04	0.98	CGRaBS J1147−3812	0.99	PKS 1144−379	1.048	FSRQ
0FGL J1159.2+2912	CGRaBS J1159+2914	39.38	0.97	CGRaBS J1159+2914	0.98	4C 29.45	0.729	FSRQ
0FGL J1218.0+3006	CGRaBS J1217+3007	31.80	0.96	B2 1215+30	1.00	B2 1215+30	0.130	BLLac
0FGL J1221.7+2814	CGRaBS J1221+2813	36.82	0.97	W Com	1.00	W Com	0.102	BLLac
0FGL J1229.1+0202	CGRaBS J1229+0203	73.53	1.00	3C 273	1.00	3C 273	0.158	FSRQ
0FGL J1246.6−2544	CGRaBS J1246−2547	43.45	0.98	CGRaBS J1246−2547	0.99	PKS 1244−255	0.635	FSRQ
0FGL J1253.4+5300	CRATES J1253+5301	43.34	0.98	S4 1250+53	1.00	S4 1250+53	· · ·	BLLac
0FGL J1256.1−0547	CGRaBS J1256−0547	71.21	1.00	3C279	1.00	3C 279	0.536	FSRQ
0FGL J1310.6+3220	CGRaBS J1310+3220	55.91	0.99	CGRaBS J1310+3220	0.99	B2 1308+32	0.997	FSRQ

Table 1—Continued

LAT Name	FoM Source Name	FoM	FoM Prob.	*gtsrcid* Source Name	*gtsrcid* Prob.	Other Names	z	Class
0FGL J1325.4−4303	BZU J1325−4301	75.23	1.00	NGC 5128	1.00	NGC 5128, Cen A	0.002	RG
0FGL J1331.7−0506	CGRaBS J1332−0509	44.64	0.98	CGRaBS J1332−0509	0.93	PKS 1329−049	2.150	FSRQ
0FGL J1333.3+5058	CLASS J1333+5057	21.52	0.94	···	···	···	1.362	FSRQ
0FGL J1355.0−1044	CRATES J1354−1041	22.52	0.94	BZUJ1354−1041	0.84	PKS 1352−104	0.330	FSRQ
0FGL J1427.1+2347	CRATES J1427+2347	19.69	0.94	PKS 1424+240	1.00	PKS 1424+240	···	BLLac
0FGL J1457.6−3538	CGRaBS J1457−3539	26.03	0.95	CGRaBS J1457−3539	0.99	PKS 1454−354	1.424	FSRQ
0FGL J1504.4+1030	CGRaBS J1504+1029	48.85	0.98	CGRaBS J1504+1029	1.00	PKS 1502+106	1.839	FSRQ
0FGL J1511.2−0536	PKS 1508−05	10.27	0.90	BZQJ1510−0543	0.73	PKS 1508−05	1.185	FSRQ
0FGL J1512.7−0905	PKS 1510−08	74.49	1.00	BZQJ1512−0905	0.98	PKS 1510−08	0.360	FSRQ
0FGL J1517.9−2423	CGRaBS J1517−2422	19.18	0.94	AP Lib	1.00	AP Lib	0.048	BLLac
0FGL J1522.2+3143	CGRaBS J1522+3144	51.06	0.99	CGRaBS J1522+3144	1.00	TXS 1520+319	1.487	FSRQ
0FGL J1543.1+6130	CRATES J1542+6129	45.22	0.98	RXS J15429+6129	1.00	RXS J15429+6129	···	BLLac
0FGL J1553.4+1255	CRATES J1553+1256	26.38	0.95	PKS 1551+130	0.85	PKS 1551+130	1.308	FSRQ
0FGL J1555.8+1110	CGRaBS J1555+1111	44.23	0.98	PG 1553+11	1.00	PG 1553+11	0.360	BLLac
0FGL J1625.8−2527	CGRaBS J1625−2527	56.82	0.99	PKS 1622−253	0.99	PKS 1622−253	0.786	FSRQ
0FGL J1635.2+3809	CGRaBS J1635+3808	54.10	0.99	CRATESJ1635+3808	0.99	4C +38.41	1.814	FSRQ
0FGL J1653.9+3946	CGRaBS J1653+3945	59.08	0.99	Mrk 501	1.00	Mrk 501	0.033	BLLac
0FGL J1719.3+1746	CGRaBS J1719+1745	40.87	0.98	PKS 1717+177	1.00	PKS 1717+177	0.137	BLLac
0FGL J1751.5+0935	CGRaBS J1751+0939	19.73	0.94	CGRaBS J1751+0939	0.99	OT 081	0.322	BLLac
0FGL J1802.2+7827	CGRaBS J1800+7828	28.07	0.96	CGRaBS J1800+7828	0.99	S5 1803+78	0.680	BLLac
0FGL J1847.8+3223	CGRaBS J1848+3219	12.76	0.92	CGRaBS J1848+3219	0.94	TXS 1846+322	0.798	FSRQ
0FGL J1849.4+6706	CGRaBS J1849+6705	53.89	0.99	CGRaBS J1849+6705	1.00	S4 1849+67	0.657	FSRQ
0FGL J1911.2−2011	CGRaBS J1911−2006	23.51	0.95	CGRaBS J1911−2006	0.97	PKS 1908−201	1.119	FSRQ
0FGL J1923.3−2101	CGRaBS J1923−2104	37.72	0.97	CGRaBS J1923−2104	0.97	TXS 1920−211	0.874	FSRQ
0FGL J2000.2+6506	CGRaBS J1959+6508	19.12	0.94	1ES 1959+650	1.00	1ES 1959+650	0.047	BLLac
0FGL J2009.4−4850	CGRaBS J2009−4849	72.13	1.00	PKS 2005−489	1.00	PKS 2005−489	0.071	BLLac
0FGL J2025.6−0736	CRATES J2025−0735	42.71	0.98	BZQJ2025−0735	0.98	PKS 2022−07	1.388	FSRQ
0FGL J2056.1−4715	CGRaBS J2056−4714	67.00	1.00	CRATES J2055−4716	1.00	PKS 2052−47	1.491	FSRQ
0FGL J2139.4−4238	CRATES J2139−4235	13.48	0.92	MH 2136−428	1.00	MH 2136−428	···	BLLac
0FGL J2143.2+1741	CGRaBS J2143+1743	36.88	0.97	CGRaBS J2143+1743	0.96	OX 169	0.213	FSRQ
0FGL J2147.1+0931	CGRaBS J2147+0929	53.97	0.99	CGRaBS J2147+0929	0.99	PKS 2144+092	1.113	FSRQ
0FGL J2157.5+3125	CGRaBS J2157+3127	54.48	0.99	CGRaBS J2157+3127	0.97	B2 2155+31	1.486	FSRQ
0FGL J2158.8−3014	CGRaBS J2158−3013	54.87	0.99	CGRaBS J2158−3013	1.00	PKS 2155−304	0.116	BLLac
0FGL J2202.4+4217	BZB J2202+4216	45.62	0.98	BZB J2139−4239	1.00	BL Lacertae	0.069	BLLac
0FGL J2203.2+1731	CGRaBS J2203+1725	23.91	0.95	CGRaBS J2203+1725	0.93	PKS 2201+171	1.076	FSRQ
0FGL J2207.0−5347	CGRaBS J2207−5346	39.56	0.97	CGRaBS J2207−5346	0.99	PKS 2204−54	1.215	FSRQ
0FGL J2229.8−0829	CGRaBS J2229−0832	42.99	0.98	CGRaBS J2229−0832	0.99	PHL 5225	1.560	FSRQ
0FGL J2232.4+1141	BZQ J2232+1143	45.97	0.98	BZQ J2232+1143	1.00	CTA 102	1.037	FSRQ
0FGL J2254.0+1609	CGRaBS J2253+1608	70.34	1.00	CGRaBS J2253+1608	1.00	3C 454.3	0.859	FSRQ
0FGL J2325.3+3959	CRATES J2325+3957	29.25	0.96	B3 2322+396	1.00	B3 2322+396	···	BLLac
0FGL J2327.3+0947	CGRaBS J2327+0940	21.12	0.94	CGRaBS J2327+0940	0.93	PKS 2325+093	1.843	FSRQ
0FGL J2345.5−1559	CGRaBS J2345−1555	30.19	0.96	CGRaBS J2345−1555	0.93	PMN J2345−1555	0.621	FSRQ

[***] All these source have a flat radio spectrum but there are no other data reported in literature which allow to classify them either as FSRQs or BL Lacs.

Table 2. The low-confidence association Bright AGN List

	FoM			*gtsrcid*				
LAT Name	Source Name	FoM	Prob.	Source Name	Prob.	Other Names	z	Class
0FGL J0100.2+0750	CRATES J0100+0745	5.12	0.78	···	···	···	0.000	Unc***
0FGL J0238.4+2855	CGRaBS J0237+2848	7.67	0.89	CGRaBS J0237+2848	0.88	B2 0234+28	1.213	FSRQ
0FGL J0407.6−3829	CRATES J0406−3826	3.00	0.61	···	···	PKS 0405−385	1.285	Unc***
0FGL J0412.9−5341	CRATES J0413−5332	1.92	0.46	···	0.00	···	···	Unc***
0FGL J0423.1−0112	CGRaBS J0423−0120	4.26	0.72	CRATESJ0423−0120	0.84	PKS 0420−014	0.915	FSRQ
0FGL J0909.7+0145	CGRaBS J0909+0200	4.16	0.71	PKS 0907+022	0.87	PKS 0907+022	···	BLLac
0FGL J1034.0+6051	CRATES J1032+6051	5.22	0.79	···	···	···	1.064	FSRQ
0FGL J1248.7+5811	···	···	···	PG 1246+586	0.86	···	···	BLLac
0FGL J1625.9−2423	CRATES J1627−2426	2.33	0.53	···	···	···	···	Unc***
0FGL J1641.4+3939	CLASS J1641+3935	6.22	0.85	···	···	···	0.539	FSRQ
0FGL J2017.2+0602	CLASS J2017+0603	7.03	0.88	···	···	···	···	Unc***

***All these sources have a flat radio spectrum but there are no other data reported in literature which allow to classify them either as FSRQs or BL Lacs.

Table 3. The *Fermi* – LAT $|b| > 10°$ Bright AGN List

LAT Name	R.A.	Dec	l	b	$\sqrt{TS}$	Γ[a]	F_{100}[b]	F_{peak}[c]	F_{25}[d]	Var.
0FGL J0017.4-0503	4.358	−5.054	101.273	−66.485	14.7	2.71 ± 0.14	13.9 ± 2.4	34.8 ± 6.5	12.1 ± 1.4	T
0FGL J0033.6-1921	8.401	−19.360	94.215	−81.220	10.7	1.70 ± 0.14	1.6 ± 0.4	2.9 ± 1.3	0.4 ± 0.1†	···
0FGL J0050.5-0928	12.637	−9.470	122.209	−72.341	20.5	2.15 ± 0.08	10.2 ± 1.4	19.0 ± 4.0	8.8 ± 1.3	T
0FGL J0051.1-0647	12.796	−6.794	122.751	−69.666	15.7	2.22 ± 0.11	8.5 ± 1.5	19.7 ± 4.4	7.2 ± 1.4	T
0FGL J0100.2+0750	15.051	7.844	126.716	−54.963	11.1	1.80 ± 0.16	1.9 ± 0.7	3.9 ± 1.7	0.3 ± 0.1†	···
0FGL J0112.1+2247	18.034	22.789	129.148	−39.832	17.6	2.10 ± 0.09	7.4 ± 1.2	12.6 ± 2.7	6.0 ± 0.7	···
0FGL J0118.7-2139	19.676	−21.656	172.990	−81.728	17.8	2.32 ± 0.10	9.6 ± 1.4	21.4 ± 4.5	7.6 ± 1.1	T
0FGL J0120.5-2703	20.128	−27.056	213.951	−83.529	11.8	1.99 ± 0.14	3.2 ± 0.8	6.7 ± 2.3	2.6 ± 0.8	···
0FGL J0136.6+3903	24.163	39.066	132.446	−22.969	12.5	1.65 ± 0.13	1.8 ± 0.5	4.7 ± 1.5	0.5 ± 0.1†	···
0FGL J0137.1+4751	24.285	47.854	130.818	−14.317	18.8	2.20 ± 0.09	10.9 ± 1.7	18.6 ± 4.5	10.8 ± 1.6	T
0FGL J0144.5+2709	26.142	27.159	137.248	−34.231	10.4	2.22 ± 0.14	5.4 ± 1.3	12.7 ± 3.8	2.0 ± 0.5	···
0FGL J0145.1-2728	26.289	−27.478	217.694	−78.067	13.4	2.55 ± 0.14	9.2 ± 1.7	26.3 ± 5.4	9.4 ± 1.3	T
0FGL J0204.8-1704	31.219	−17.068	186.072	−70.274	16.6	2.48 ± 0.11	11.1 ± 1.7	18.9 ± 3.9	10.7 ± 1.3	···
0FGL J0210.8-5100	32.706	−51.013	276.083	−61.776	34.1	2.28 ± 0.06	24.4 ± 2.0	76.2 ± 6.9	22.8 ± 1.2	T
0FGL J0217.8+0146	34.467	1.768	162.139	−54.389	21.7	2.13 ± 0.08	10.2 ± 1.3	16.5 ± 3.8	9.8 ± 1.2	T
0FGL J0220.9+3607	35.243	36.121	142.504	−23.325	12.3	2.61 ± 0.16	11.0 ± 2.4	22.5 ± 6.1	10.9 ± 1.3	···
0FGL J0222.6+4302	35.653	43.043	140.132	−16.763	47.4	1.97 ± 0.04	25.9 ± 1.6	49.6 ± 4.8	26.6 ± 1.4	T
0FGL J0229.5-3640	37.375	−36.681	243.801	−67.189	19.2	2.57 ± 0.11	15.8 ± 2.1	34.1 ± 6.2	14.1 ± 1.5	T
0FGL J0238.4+2855	39.600	28.923	149.521	−28.368	10.9	2.49 ± 0.15	9.0 ± 2.0	24.7 ± 5.9	8.6 ± 1.6	···
0FGL J0238.6+1636	39.663	16.613	156.775	−39.112	85.7	2.05 ± 0.02	72.6 ± 2.5	104.8 ± 7.1	67.6 ± 2.2	T
0FGL J0245.6-4656	41.423	−46.934	262.019	−60.098	11.4	2.34 ± 0.15	6.2 ± 1.5	12.4 ± 4.0	5.6 ± 0.8	···
0FGL J0303.7-2410	45.940	−24.176	214.764	−60.119	12.3	2.01 ± 0.13	3.8 ± 0.9	8.0 ± 2.8	2.9 ± 0.9	···
0FGL J0320.0+4131	50.000	41.524	150.601	−13.230	29.7	2.17 ± 0.06	22.1 ± 1.9	35.9 ± 5.3	18.2 ± 1.4	T
0FGL J0334.1-4006	53.546	−40.107	244.710	−54.088	13.2	2.15 ± 0.12	5.3 ± 1.1	11.2 ± 3.1	4.9 ± 1.4	···
0FGL J0349.8-2102	57.465	−21.046	214.385	−49.035	21.2	2.55 ± 0.09	19.2 ± 2.3	27.8 ± 5.0	17.3 ± 1.6	···
0FGL J0407.6-3829	61.923	−38.491	241.360	−47.751	13.5	2.31 ± 0.13	7.5 ± 1.5	22.2 ± 4.1	6.9 ± 1.3	T
0FGL J0412.9-5341	63.230	−53.686	263.001	−44.716	10.7	2.30 ± 0.15	5.4 ± 1.3	12.3 ± 3.8	6.0 ± 1.3	···
0FGL J0423.1-0112	65.785	−1.204	195.131	−33.092	11.5	2.38 ± 0.16	8.1 ± 2.2	13.4 ± 4.0	10.5 ± 3.1	···
0FGL J0428.7-3755	67.193	−37.923	240.689	−43.597	39.6	2.14 ± 0.05	24.5 ± 1.8	31.5 ± 4.7	23.1 ± 1.6	···
0FGL J0449.7-4348	72.435	−43.815	248.780	−39.859	28.4	2.01 ± 0.06	12.0 ± 1.3	21.1 ± 4.2	12.2 ± 1.4	···
0FGL J0457.1-2325	74.288	−23.432	223.739	−34.880	52.3	2.23 ± 0.04	41.8 ± 2.3	64.2 ± 6.4	36.6 ± 1.8	T
0FGL J0507.9+6739	76.985	67.650	143.772	15.905	13.2	1.67 ± 0.18	1.7 ± 0.8	5.2 ± 1.7	0.3 ± 0.1†	···
0FGL J0516.2-6200	79.063	−62.000	271.376	−34.834	11.2	2.17 ± 0.17	5.4 ± 1.7	11.1 ± 3.3	0.4 ± 0.1†	···
0FGL J0531.0+1331	82.761	13.528	191.385	−10.992	17.3	2.54 ± 0.09	24.3 ± 2.9	39.5 ± 6.7	23.6 ± 2.1	T
0FGL J0538.8-4403	84.725	−44.062	250.057	−31.075	48.6	2.19 ± 0.04	37.6 ± 2.2	49.7 ± 5.6	34.3 ± 1.8	T
0FGL J0654.3+4513	103.590	45.220	171.228	19.369	29.2	2.32 ± 0.06	23.8 ± 2.1	56.4 ± 7.2	20.3 ± 1.6	T
0FGL J0654.3+5042	103.592	50.711	165.676	21.107	15.6	2.00 ± 0.10	5.5 ± 1.1	9.5 ± 2.6	4.9 ± 1.3	T
0FGL J0700.0-6611	105.016	−66.199	276.778	−23.809	10.1	1.98 ± 0.14	3.9 ± 1.0	8.7 ± 2.6	0.4 ± 0.1 †	···
0FGL J0712.9+5034	108.231	50.575	166.688	23.900	11.2	2.04 ± 0.14	3.9 ± 1.1	10.5 ± 2.7	3.3 ± 0.7	···
0FGL J0714.2+1934	108.552	19.574	197.685	13.648	15.0	2.35 ± 0.10	10.7 ± 1.6	27.0 ± 5.0	10.0 ± 1.6	T
0FGL J0719.4+3302	109.869	33.037	185.139	19.855	12.3	2.37 ± 0.15	7.8 ± 1.7	20.8 ± 4.9	7.5 ± 1.5	T
0FGL J0722.0+7120	110.508	71.348	143.976	28.029	34.4	2.08 ± 0.05	16.4 ± 1.4	29.0 ± 4.2	17.0 ± 1.6	T
0FGL J0738.2+1738	114.575	17.634	201.933	18.081	11.9	2.10 ± 0.14	4.6 ± 1.1	7.5 ± 2.4	3.6 ± 1.4	···
0FGL J0818.3+4222	124.579	42.367	178.244	33.409	20.9	2.07 ± 0.08	9.6 ± 1.3	14.5 ± 2.9	7.0 ± 1.1	···
0FGL J0824.9+5551	126.239	55.859	161.981	35.142	10.6	2.81 ± 0.20	11.4 ± 2.9	42.0 ± 8.1	10.8 ± 1.3	T
0FGL J0855.4+2009	133.857	20.162	206.810	35.974	15.1	2.31 ± 0.11	9.0 ± 1.5	19.0 ± 4.1	7.8 ± 1.3	···
0FGL J0909.7+0145	137.446	1.757	228.640	31.262	11.6	2.67 ± 0.16	10.4 ± 2.1	22.9 ± 6.1	9.5 ± 0.3	···
0FGL J0921.2+4437	140.320	44.617	175.809	44.876	15.2	2.35 ± 0.12	8.6 ± 1.5	15.7 ± 4.2	9.2 ± 1.4	···
0FGL J0948.3+0019	147.077	0.317	236.530	38.549	12.8	2.60 ± 0.14	12.1 ± 2.2	29.2 ± 5.7	9.1 ± 1.4	T
0FGL J0957.6+5522	149.424	55.375	158.605	47.939	24.0	2.01 ± 0.07	8.7 ± 1.1	12.9 ± 3.0	9.2 ± 1.3	···
0FGL J1012.9+2435	153.241	24.598	207.897	54.406	12.4	2.22 ± 0.12	6.1 ± 1.2	10.9 ± 3.6	4.5 ± 0.9	T
0FGL J1015.2+4927	153.809	49.463	165.473	52.727	23.8	1.73 ± 0.07	4.9 ± 0.7	7.1 ± 1.7	8.9 ± 1.5	···
0FGL J1015.9+0515	153.991	5.254	236.457	47.036	20.6	2.20 ± 0.08	11.7 ± 1.5	21.8 ± 4.5	13.1 ± 1.5	T
0FGL J1034.0+6051	158.504	60.853	147.765	49.122	14.8	2.48 ± 0.13	9.3 ± 1.7	22.0 ± 4.7	7.5 ± 1.3	···
0FGL J1053.7+4926	163.442	49.449	160.309	58.263	10.1	1.42 ± 0.20	0.5 ± 0.3	1.8 ± 0.9	0.2 ± 0.1†	···
0FGL J1054.5+2212	163.626	22.215	216.968	63.049	11.2	2.24 ± 0.15	4.9 ± 1.3	10.8 ± 3.3	4.3 ± 1.0	···
0FGL J1057.8+0138	164.451	1.643	251.219	52.709	10.3	2.20 ± 0.17	5.0 ± 1.4	10.7 ± 2.8	9.2 ± 1.7	···
0FGL J1058.9+5629	164.731	56.488	149.521	54.442	12.0	2.11 ± 0.14	3.9 ± 1.0	8.3 ± 2.7	5.0 ± 1.8	···
0FGL J1100.2-8000	165.057	−80.012	298.047	−18.212	12.1	2.71 ± 0.16	17.1 ± 3.8	38.4 ± 8.5	11.1 ± 2.2	T
0FGL J1104.5+3811	166.137	38.187	179.868	65.056	47.1	1.77 ± 0.04	15.3 ± 1.1	20.9 ± 3.1	15.9 ± 1.3	···
0FGL J1129.8-1443	172.454	−14.727	275.133	43.694	10.5	2.69 ± 0.18	9.9 ± 2.4	25.8 ± 5.8	10.8 ± 1.6	···
0FGL J1146.7-3808	176.689	−38.149	289.170	22.988	10.4	2.21 ± 0.14	5.7 ± 1.4	7.5 ± 2.8	3.5 ± 1.2	···
0FGL J1159.2+2912	179.800	29.216	199.605	78.307	14.6	2.47 ± 0.13	10.3 ± 1.8	16.0 ± 3.8	9.4 ± 1.0	···
0FGL J1218.0+3006	184.517	30.108	188.826	82.097	27.4	1.89 ± 0.06	9.7 ± 1.1	40.9 ± 4.7	10.4 ± 1.0	T
0FGL J1221.7+2814	185.439	28.243	201.593	83.336	24.0	1.93 ± 0.07	8.3 ± 1.1	17.2 ± 3.5	7.5 ± 0.9	T
0FGL J1229.1+0202	187.287	2.045	289.975	64.355	52.0	2.71 ± 0.05	75.2 ± 4.3	137.0 ± 13.0	65.5 ± 2.6	T

Table 3—Continued

LAT Name	R.A.	Dec	l	b	$\sqrt{TS}$	Γ[a]	F_{100}[b]	F_{peak}[c]	F_{25}[d]	Var.
0FGL J1246.6-2544	191.655	−25.734	301.571	37.125	11.7	2.24 ± 0.14	6.8 ± 1.6	15.3 ± 4.3	7.6 ± 1.4	···
0FGL J1248.7+5811	192.189	58.191	123.617	58.934	14.3	1.95 ± 0.11	3.8 ± 0.8	8.0 ± 2.4	7.4 ± 1.6	···
0FGL J1253.4+5300	193.369	53.001	122.229	64.125	12.1	2.17 ± 0.14	4.7 ± 1.1	9.1 ± 2.6	5.6 ± 1.5	···
0FGL J1256.1-0547	194.034	−5.800	305.081	57.052	36.8	2.35 ± 0.05	31.5 ± 2.3	46.3 ± 6.8	29.7 ± 1.8	T
0FGL J1310.6+3220	197.656	32.339	85.458	83.331	27.3	2.25 ± 0.07	15.5 ± 1.6	37.3 ± 4.6	16.4 ± 1.1	T
0FGL J1325.4-4303	201.353	−43.062	309.501	19.376	12.4	2.91 ± 0.18	21.5 ± 4.5	32.3 ± 8.0	22.2 ± 2.4	···
0FGL J1331.7-0506	202.935	−5.112	321.247	56.320	14.3	2.59 ± 0.12	13.0 ± 2.1	33.0 ± 5.9	10.7 ± 1.2	T
0FGL J1333.3+5058	203.331	50.973	107.300	64.865	12.4	2.40 ± 0.14	7.2 ± 1.5	13.7 ± 4.6	9.1 ± 1.3	T
0FGL J1355.0-1044	208.764	−10.735	327.221	49.113	11.5	2.37 ± 0.15	7.6 ± 1.8	34.4 ± 5.5	8.7 ± 1.3	T
0FGL J1427.1+2347	216.794	23.785	29.472	68.166	24.1	1.80 ± 0.07	6.2 ± 0.8	8.7 ± 2.2	5.1 ± 1.0	···
0FGL J1457.6-3538	224.407	−35.639	329.936	20.530	39.6	2.24 ± 0.05	36.6 ± 2.4	77.2 ± 7.1	32.1 ± 0.5	T
0FGL J1504.4+1030	226.115	10.505	11.409	54.577	88.2	2.17 ± 0.02	81.4 ± 2.7	260.0 ± 15.0	69.3 ± 2.1	T
0FGL J1511.2-0536	227.814	−5.613	354.099	42.948	10.8	2.41 ± 0.15	8.8 ± 2.1	16.2 ± 4.4	8.6 ± 1.7	···
0FGL J1512.7-0905	228.196	−9.093	351.282	40.153	45.0	2.48 ± 0.05	55.8 ± 3.3	165.9 ± 11.7	50.6 ± 2.3	T
0FGL J1517.9-2423	229.496	−24.395	340.724	27.521	12.3	1.94 ± 0.14	4.1 ± 1.2	7.0 ± 2.4	5.2 ± 0.6	···
0FGL J1522.2+3143	230.552	31.726	50.143	57.014	34.3	2.39 ± 0.06	25.7 ± 2.1	42.0 ± 5.1	22.2 ± 1.5	T
0FGL J1543.1+6130	235.784	61.504	95.383	45.370	10.5	2.00 ± 0.15	2.5 ± 0.7	4.3 ± 1.7	3.3 ± 1.4	···
0FGL J1553.4+1255	238.368	12.922	23.746	45.225	23.7	2.23 ± 0.07	16.1 ± 1.8	33.6 ± 5.6	15.6 ± 2.2	T
0FGL J1555.8+1110	238.951	11.181	21.911	43.941	31.5	1.70 ± 0.06	8.0 ± 1.0	11.6 ± 2.3	10.2 ± 2.0	···
0FGL J1625.8-2527	246.470	−25.451	352.164	16.308	11.4	2.40 ± 0.15	16.0 ± 4.6	28.4 ± 8.0	19.8 ± 1.3	···
0FGL J1625.9-2423	246.494	−24.393	353.005	16.995	10.1	2.46 ± 0.14	19.9 ± 5.1	32.1 ± 8.1	10.7 ± 0.9	···
0FGL J1635.2+3809	248.821	38.158	61.118	42.333	27.3	2.44 ± 0.07	22.0 ± 2.2	49.8 ± 6.0	17.6 ± 1.3	T
0FGL J1641.4+3939	250.355	39.666	63.239	41.239	17.7	2.43 ± 0.10	13.4 ± 2.1	33.7 ± 6.3	12.7 ± 1.4	T
0FGL J1653.9+3946	253.492	39.767	63.612	38.841	19.0	1.70 ± 0.09	3.1 ± 0.6	6.9 ± 1.8	3.3 ± 0.8	···
0FGL J1719.3+1746	259.830	17.768	39.553	28.080	23.3	1.84 ± 0.07	6.9 ± 0.9	15.0 ± 3.0	6.3 ± 1.2	T
0FGL J1751.5+0935	267.893	9.591	34.867	17.614	23.1	2.27 ± 0.07	18.4 ± 2.1	41.4 ± 6.3	17.8 ± 1.9	T
0FGL J1802.2+7827	270.567	78.466	110.026	28.990	12.6	2.25 ± 0.14	6.0 ± 1.4	11.1 ± 3.1	5.9 ± 1.3	···
0FGL J1847.8+3223	281.954	32.385	62.065	14.838	16.0	2.37 ± 0.10	14.7 ± 2.4	28.0 ± 4.9	9.4 ± 0.6	T
0FGL J1849.4+6706	282.365	67.102	97.503	25.027	28.0	2.17 ± 0.06	15.9 ± 1.5	28.8 ± 4.1	14.9 ± 1.5	T
0FGL J1911.2-2011	287.813	−20.186	16.818	−13.266	20.0	2.43 ± 0.08	22.5 ± 2.7	52.3 ± 7.2	18.7 ± 0.8	T
0FGL J1923.3-2101	290.840	−21.031	17.205	−16.199	16.4	2.31 ± 0.10	13.1 ± 2.0	41.6 ± 6.1	11.3 ± 0.6	T
0FGL J2000.2+6506	300.053	65.105	97.974	17.630	15.8	1.86 ± 0.11	4.2 ± 1.0	6.3 ± 2.1	3.4 ± 1.3	···
0FGL J2009.4-4850	302.363	−48.843	350.361	−32.607	10.9	1.85 ± 0.14	2.9 ± 0.9	5.5 ± 2.1	3.0 ± 0.6	···
0FGL J2017.2+0602	304.302	6.048	48.596	−15.991	12.7	1.87 ± 0.12	3.7 ± 0.9	6.6 ± 2.3	$0.6 \pm 0.1^{\dagger}$	···
0FGL J2025.6-0736	306.415	−7.611	36.883	−24.389	50.6	2.30 ± 0.04	48.0 ± 2.6	73.6 ± 7.1	43.0 ± 2.0	T
0FGL J2056.1-4715	314.034	−47.251	352.586	−40.358	12.5	2.56 ± 0.15	11.1 ± 2.3	21.1 ± 5.2	10.7 ± 1.7	···
0FGL J2139.4-4238	324.865	−42.642	358.237	−48.332	20.1	2.01 ± 0.08	8.0 ± 1.2	13.1 ± 3.0	7.7 ± 1.3	···
0FGL J2143.2+1741	325.807	17.688	72.016	−26.051	14.5	2.57 ± 0.12	14.1 ± 2.2	30.7 ± 6.2	12.0 ± 1.7	···
0FGL J2147.1+0931	326.777	9.519	65.805	−32.236	19.9	2.53 ± 0.10	16.6 ± 2.1	34.7 ± 6.1	16.6 ± 1.6	T
0FGL J2157.5+3125	329.384	31.431	84.747	−18.258	10.0	2.41 ± 0.15	7.5 ± 1.7	13.9 ± 3.9	7.3 ± 1.5	···
0FGL J2158.8-3014	329.704	−30.237	17.711	−52.236	43.9	1.85 ± 0.04	18.1 ± 1.2	29.2 ± 3.6	18.5 ± 1.4	T
0FGL J2202.4+4217	330.622	42.299	92.569	−10.398	12.3	2.24 ± 0.12	8.5 ± 1.8	12.8 ± 4.3	8.0 ± 2.0	···
0FGL J2203.2+1731	330.815	17.532	75.715	−29.529	12.7	2.25 ± 0.13	6.9 ± 1.4	17.0 ± 3.5	8.3 ± 1.6	T
0FGL J2207.0-5347	331.765	−53.786	339.948	−49.832	12.4	2.65 ± 0.17	11.5 ± 2.5	54.6 ± 8.0	11.1 ± 1.8	T
0FGL J2229.8-0829	337.452	−8.495	55.326	−51.701	16.8	2.67 ± 0.12	15.9 ± 2.4	27.7 ± 5.7	12.0 ± 0.4	···
0FGL J2232.4+1141	338.117	11.690	77.372	−38.592	15.2	2.61 ± 0.12	14.0 ± 2.3	24.6 ± 6.2	11.2 ± 1.3	···
0FGL J2254.0+1609	343.502	16.151	86.125	−38.187	149.1	2.41 ± 0.02	246.1 ± 5.2	385.8 ± 20.5	221.6 ± 4.3	T
0FGL J2325.3+3959	351.334	39.993	105.532	−19.952	11.4	1.89 ± 0.13	2.8 ± 0.8	11.0 ± 2.7	1.3 ± 0.4	T
0FGL J2327.3+0947	351.833	9.794	91.159	−47.821	17.1	2.73 ± 0.12	18.3 ± 2.6	51.0 ± 8.4	15.8 ± 1.6	T
0FGL J2345.5-1559	356.389	−15.985	65.677	−71.092	15.5	2.42 ± 0.12	10.5 ± 1.7	22.3 ± 4.3	10.3 ± 1.3	T

[a]Spectral index derived from a single power-law fit over the 0.2-100 GeV energy range

[b]Flux ($E > 100$ MeV, in 10^{-8} ph cm^{-2} s^{-1}) derived from a single power-law fit over the 0.2-100 GeV energy range

[c]Weekly averaged peak flux ($E > 100$ MeV) in 10^{-8} ph cm^{-2} s^{-1}

[d]Flux ($E > 100$ MeV, in 10^{-8} ph cm^{-2} s^{-1}) obtained by adding the fluxes estimated in the two energy ranges 0.1− 1 GeV and 1− 100 GeV

†Flux at $E > 1$ GeV in 10^{-8} ph cm^{-2} s^{-1}. For these sources, only an upper limit is obtained for the 0.1−1 GeV flux (see Abdo et al. (2009c)).

Table 4. Sources in both *Fermi*-LAT and *EGRET* samples

LAT Name	*EGRET* Name	F^F_{mean} [a]	F^F_{peak}	index^F	F^E_{100} [a]	F^E_{peak}	index^E	Type
0FGL J0210.8−5100	J0210−5055	24.3	76.2	2.28	85.5	134.0	1.99	FSRQ
0FGL J0222.6+4302	J0222+4253	25.8	49.6	1.96	18.7	25.3	2.01	BLLac
0FGL J0238.6+1636	J0237+1635	72.5	104.	2.05	25.9	65.1	1.85	BLLac
0FGL J0423.1−0112	J0422−0102	8.0	13.3	2.37	16.3	81.7	2.44	FSRQ
0FGL J0457.1−2325	J0456−2338	41.7	64.2	2.23	8.1	18.8	3.14	FSRQ
0FGL J0516.2−6200	J0512−6150	5.3	11.1	2.17	7.2	28.8	2.40	Unc
0FGL J0531.0+1331	J0530+1323	24.3	39.4	2.54	93.5	351.0	2.46	FSRQ
0FGL J0538.8−4403	J0540−4402	37.6	49.6	2.18	25.3	91.1	2.41	BLLac
0FGL J0722.0+7120	J0721+7120	16.3	29.0	2.07	17.8	31.8	2.19	BLLac
0FGL J0738.2+1738	J0737+1721	4.6	7.46	2.10	16.4	37.5	2.60	BLLac
0FGL J0855.4+2009	J0853+1941	8.9	18.9	2.30	10.6	15.8	2.03	BLLac
0FGL J0921.2+4437	J0917+4427	8.6	15.6	2.34	13.8	40.8	2.19	FSRQ
0FGL J0957.6+5522	J0952+5501	8.7	12.8	2.01	9.1	47.2	2.12	FSRQ
0FGL J1104.5+3811	J1104+3809	15.3	20.9	1.76	13.9	27.1	1.57	BLLac
0FGL J1159.2+2912	J1200+2847	10.3	16.0	2.47	7.5	163.0	1.73	FSRQ
0FGL J1229.1+0202	J1229+0210	75.2	136.	2.71	15.4	53.6	2.58	FSRQ
0FGL J1256.1−0548	J1255−0549	31.5	46.3	2.34	74.2	267.0	1.96	FSRQ
0FGL J1325.4−4303	J1324−4314	21.4	32.3	2.90	13.6	38.4	2.58	RG (CenA)
0FGL J1333.3+5058	J1337+5029	7.2	13.7	2.4	9.2	26.8	1.83	FSRQ
0FGL J1457.6−3538	J1500−3509	36.5	77.2	2.24	10.9	40.7	2.99	FSRQ
0FGL J1512.7−0905	J1512−0849	55.8	165.	2.47	18.0	51.1	2.47	FSRQ
0FGL J1517.9−2423	J1517−2538	4.1	6.96	1.93	8.4	53.3	2.66	BLLac
0FGL J1625.8−2527	J1626−2519	16.0	28.4	2.39	21.3	90.2	2.21	FSRQ
0FGL J1625.9−2423	J1627−2419	19.9	32.1	2.45	15.8	55.2	2.21	Unc
0FGL J1635.2+3809	J1635+3813	22.0	49.7	2.43	58.4	108.0	2.15	FSRQ
0FGL J1802.6−3939[b]	J1800−3955	25.4	64.0	2.23	9.8	189.0	3.10	Unc
0FGL J1833.4−2106[b]	J1832−2110	42.0	56.8	2.61	26.6	99.3	2.59	FSRQ
0FGL J1911.2−2011	J1911−2000	22.4	52.2	2.42	17.5	47.6	2.39	FSRQ
0FGL J1923.3−2101	J1921−2015	13.0	41.6	2.31	4.6	31.0	2.10	FSRQ
0FGL J2025.6−0736	J2025−0744	47.9	73.5	2.30	21.2	74.5	2.38	BLLac
0FGL J2056.1−4715	J2055−4716	11.0	21.0	2.55	9.6	35.0	2.04	FSRQ
0FGL J2158.8−3014	J2158−3023	18.0	29.1	1.85	13.2	30.4	2.35	BLLac
0FGL J2202.4+4217	J2202+4217	8.4	12.8	2.23	11.1	39.9	2.60	BLLac
0FGL J2232.4+1141	J2232+1147	14.0	24.5	2.61	19.2	51.6	2.45	FSRQ
0FGL J2254.0+1609	J2254+1601	246.	385.	2.41	53.7	116.0	2.21	FSRQ

[a] 10^{-8} ph cm^{-2} s^{-1}

[b] source located at $|b| < 10^\circ$

Table 5. Correlation analysis for the radio and gamma-ray properties

Data	Method	Source type	# objects	Correlation coeff.	Chance probability[a]
$S_{8.4\,\mathrm{GHz}} - F_{>100\,\mathrm{MeV,peak}}$	Spearman rank	All	106	0.42	0.0000045
Log L_r-Log L_γ	Sp. r., partial	All	90	0.46	0.0000025
$S_{8.4\,\mathrm{GHz}} - F_{>100\,\mathrm{MeV,peak}}$	Spearman rank	FSRQ	57	0.19	0.080
Log L_r-Log L_γ	Sp. r., partial	FSRQ	57	0.34	0.0047
$S_{8.4\,\mathrm{GHz}} - F_{>100\,\mathrm{MeV,peak}}$	Spearman rank	BL Lacs	42	0.49	0.00055
Log L_r-Log L_γ	Sp. r., partial	BL Lacs	30	0.60	0.00023

[a]if the samples were unbiased

Table 6. Composition of the $|b| \geq 10^\circ$ sample (TS$\geq$100).

CLASS	# objects
Total	132
FSRQs	57[a]
BL Lacs	42[a]
Uncertain[b]	5[a]
Radio Galaxies	2[a]
Pulsars	7[c]
Anti-associations	4
Low confidence associations	10
Unassociated sources	5

[a]Part of the high confidence sample.

[b]Blazars with uncertain classification.

[c]Five LAT detected pulsars plus 0FGL J0025.1-7202 (47 Tuc) and 0FGL J0538.4-6856 (associated with the Large Magellan Cloud, see Abdo et al. (2009c)).

Table 7. Results of the best power-law fits to the source counts distributions. Errors within brackets are systematic uncertainties due to the incompleteness of the sample. The lower part of the table shows the results for the *flux-limited* portion of the sample.

SAMPLE	# Objects	α	A[a]	EDB fraction[b]
All[c]	121	2.59±0.12	2.62±0.24	7.2 %
Blazars	106	2.50±0.12	2.24±0.22(±0.24)	6.1 %
FSRQs	57	2.60±0.14	2.15±0.28(±0.32)	3.1 % [d]
BL Lacs	42	2.34±0.15	0.41±0.06(±0.06)	1.0 %
FSRQs	29	2.52±0.20	1.93±0.35(±0.09)	2.6 %[d]
BL Lacs	9	2.50±0.37	0.48±0.16(±0.02)	1.3 %

[a]In units of $10^4\,\mathrm{cm}^2$ s deg^{-2}.

[b]Fraction of the EGRET diffuse extragalactic background (Sreekumar et al. 1998) resolved into sources by LAT for $4 \times 10^{-8} < F_{100} < 10^{-7}$ ph cm^{-2} s^{-1}.

[c]Includes all sources except 7 pulsars and 4 anti-associated objects.

[d]The lower limit of integration in Eq. 7 has been set to 6×10^{-8} ph cm^{-2} s^{-1}.

Table 8. Results of the V/V_{MAX} test.

SAMPLE	# Objects	$<V/V_{MAX}>$
FSRQs	57	0.645 ±0.043
BL Lacs	31	0.430 ±0.055
BL Lacs[a]	42	0.472 ±0.046
BL Lacs[b]	42	0.473 ±0.046
All with $z>0$	92	0.512 ±0.031
FSRQs [c]	29	0.654 ±0.061
BL Lacs [c]	8	0.542 ±0.103

[a]For all the 11 BL Lacs without redshift, we have assumed $z = <z>$ where $<z>=0.38$.

[b]For all the 11 BL Lacs without redshift, we have drawn a redshift measurement from a Gaussian distribution with mean 0.38 and dispersion 0.34.

[c]Flux-limited sample.

Table 9. Results of best-fit power-law models to the GLFs of FSRQs in different redshift bins. The lower part of the table shows the results for the *flux-limited* portion of the sample. Errors represent the 68 % confidence level. Uncertainties within bracketes are systematic errors due to the incompleteness of the sample.

Redshift bin	# Objects	β	Normalization[a]
$z = 0.0 - 0.9$	20	1.57±0.10	2.43±0.52(±0.36)
$z = 0.9 - 1.4$	17	2.56±0.29	5.59±1.33(±0.83)
$z > 1.4$	20	2.58±0.19	13.07±2.92(±1.96)
$z = 0.0 - 0.9$	10	1.46±0.13	1.73±0.54(±0.08)
$z = 0.9 - 1.4$	8	2.65±0.48	6.62±2.34(±0.33)
$z > 1.4$	11	2.63±0.30	17.76±5.35(±0.88)

[a]Normalization of the GLF model at 10^{48} erg s^{-1} expressed in units of 10^{-11} erg^{-1} s Mpc^{-3}.

Table 10. Results of best-fit power-law models to GLFs of BL Lacs in different redshift bins. The lower part of the table shows the results for the *flux-limited* portion of the sample. Errors represent the 68 % confidence level. Uncertainties within bracketes are systematic errors due to the incompleteness of the sample.

Redshift bin	# Objects	β	Normalization[a]
z = 0.0 – 0.3	15	2.08±0.16	7.67±1.98(±3.06)
z > 0.3	16	2.10±0.11	4.75±1.18(±1.90)
z > 0.0	31	2.17±0.05	4.19±0.75(±1.67)
z > 0.0	8	1.90±0.11	6.70±2.36(±0.33)

[a]Normalization of the GLF model at 10^{48} erg s^{-1} expressed in units of 10^{-12} erg^{-1} s Mpc^{-3}.